J Mol Model (2012) 18:3587–3608
DOI 10.1007/s00894-011-1237-7

ORIGINAL PAPER

Spectroscopic investigation and hydrogen-bonding analysis of triazinones

Devadhas Arul Dhas · Isaac Hubert Joe · Solomon Dawn Dharma Roy · Sreedharan Balachandran

Received: 28 June 2011 / Accepted: 6 September 2011 / Published online: 17 February 2012
© Springer-Verlag 2011

Abstract NIR FT-Raman, FTIR and UV-vis spectra of the herbicide metamitron were recorded and analyzed. The aromaticities, equilibrium geometries, bonding features, electrostatic potentials, and harmonic vibrational wavenumbers of the monomers and dimers of triazinone derivatives were also investigated with the aid of BLYP/6-311 G(df, p) density functional theory. Features in the vibrational spectra were assigned with the aid of the VEDA.4 program. The calculated results were a good match to the experimental data obtained from FTIR, Raman, and electronic absorption spectra. Mulliken population analysis was performed on the atomic charges and the HOMO–LUMO energies were also calculated. NBO analysis highlighted the intra- and intermolecular N–H…O and C–H…O hydrogen bonds in the crystal structures of the triazinones. The solvent effect was calculated using time-dependent density functional theory in combination with the polarizable continuum model.

Electronic supplementary material The online version of this article (doi:10.1007/s00894-011-1237-7) contains supplementary material, which is available to authorized users.

D. A. Dhas · S. D. D. Roy
Department of Physics, Nesamony Memorial Christian College, Marthandam 629 165, Tamil Nadu, India

I. H. Joe (✉)
Centre for Molecular and Biophysics Research, Department of Physics, Mar Ivanios College, Thiruvananthapuram 695 015, Kerala, India
e-mail: hubertjoe@gmail.com

I. H. Joe
e-mail: hubertjoe@sancharnet.in

S. Balachandran
Department of Chemistry, M.G. College, Thiruvananthapuram 695 004, Kerala, India

Keywords Herbicide · H-bonding · Dimer · Aromaticity · ICT

Introduction

Chemical substances derived from 4-amino-1,2,4-triazin-5 (4H)-one exhibit herbicidal activity [1]. These compounds are chemically stable and can penetrate slowly through the soil, causing long-term contamination of underground drinking water resources [1]. Metamitron is used to control grasses and broad-leaved weeds in sugar and red beets, fodder beet, and certain strawberry varieties with low toxicity and low residue. It can be used to deal with crop sprouting before sowing or after sowing, and can be applied to suppress the growth of weeds throughout the growing period [2]. Metribuzin is effective against annual grasses and many broad-leaved weeds, including hard-to-control weeds. The properties of these triazinone derivatives have been studied using electrochemistry [3], photocatalytic processes [4], phototransformation [5], photoreaction [6], and IR spectroscopy [7].

Intermolecular hydrogen-bonding interactions have received much attention from both practical and theoretical perspectives, as they can determine the structures and activities of biological molecules [8–12]. Interactions of molecules with target proteins are absolutely crucial to various bioactivities, which in turn depend on the structural features of the molecules, including their hydrogen-bonding abilities. In the study described in the present paper, the structural features of three closely related triazinone derivatives—metamitron, isometamitron, and metribuzin (Fig. 1a–f)—were investigated, along with their dimers, to obtain a good understanding of their hydrogen-bonding capabilities. This investigation also

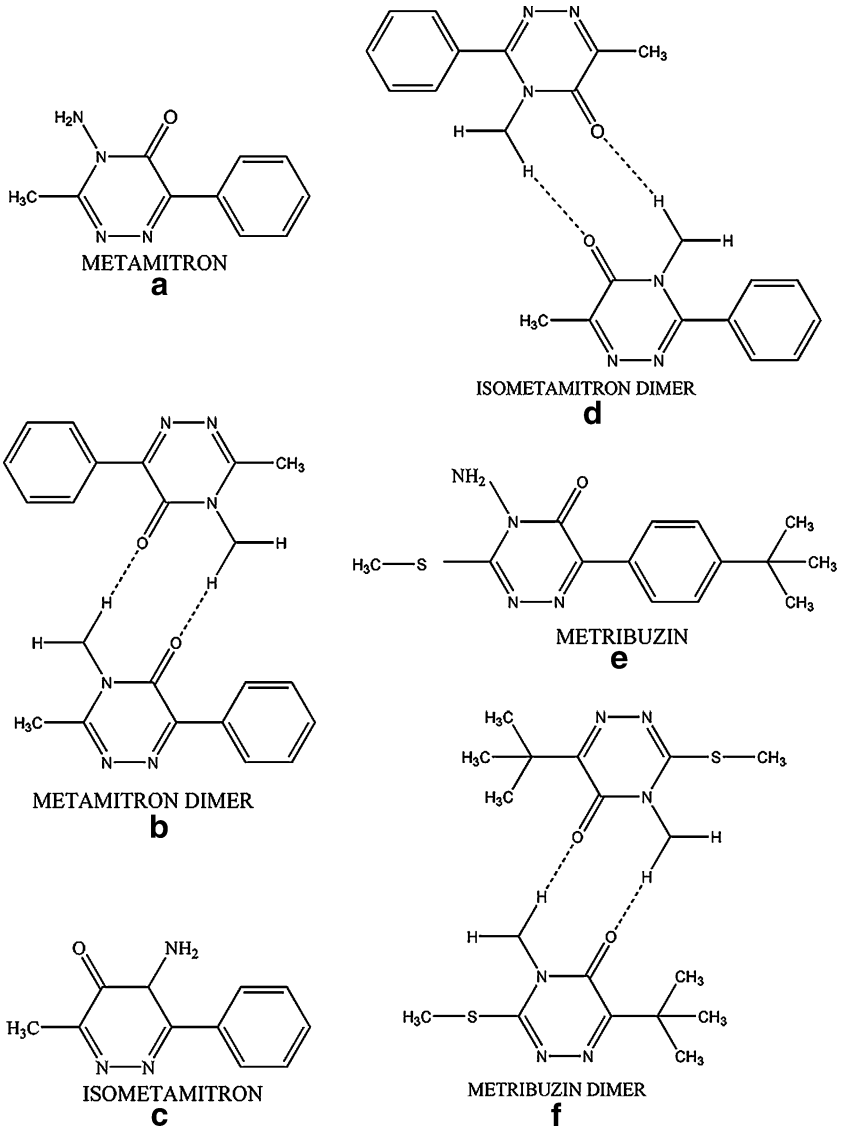

Fig. 1 **a** The structure of the metamitron monomer. **b** The structure of the metamitron dimer. **c** The structure of the isometamitron monomer. **d** The structure of the isometamitron dimer. **e** The structure of the metribuzin monomer. **f** The structure of the metribuzin dimer

explored the authenticity of the aromaticity of the heterocyclic ring, as calculated by an empirical method [13]. Vibrational spectroscopic investigations aided by quantum chemical computations have recently been used as an effective tool in the structural analysis of pesticide compounds [12]. Because they have been highly successfully used to calculate the electronic structures and energies of various compounds, density functional theory (DFT) with the BLYP/6-311 G(df, p) hybrid functional and time-dependent density functional theory using the polarized continuum model (TD-DFT/PCM) calculations were performed for these triazinone derivatives using the Gaussian 03 suite of quantum chemical codes. The vibrational characteristics of their monomers and dimers were studied using their FT-Raman, IR spectra, UV-vis spectra, HOMO and LUMO energies, as well as natural bond orbital (NBO) analysis.

Experimental details

Metamitron was purchased from Sigma–Aldrich (St. Louis, MO, USA) and used without further purification. The IR spectrum of each sample was recorded using a PerkinElmer Spectrum One FTIR spectrometer in the region 400–4000 cm^{-1}, using a KBr sample pellet. The resolution of the spectrum was 4 cm^{-1}. An NIR FT-Raman spectrum in the range 50–3500 cm^{-1} was also recorded using a powdered sample, with the 1064 nm line provided by an Nd:YAG laser employed as the excitation source, and analyzed on Bruker Vertex 70 FT-IR-RAM-II FT-Raman module. The detector was a Ge diode cooled to liquid nitrogen temperature. One thousand scans were accumulated, with a total registration time of about 30 min. The spectral resolution after apodization was 2 cm^{-1}. The upper limit for the Raman wavenumber was restricted to

3500 cm^{-1} because of the detector's sensitivity, and the lower Raman wavenumber was limited to around 50 cm^{-1} because the Rayleigh line was cut off by a notch filter. The UV-visible absorption spectrum of the sample was measured on the basis of ASTME 169–693, using a Varian Cary 100 B10 UV-visible spectrophotometer.

Computational methods

The DFT computations for the triazinone derivatives were carried out in the Gaussian 03 program package [14] using "ultrafine" integration grids. The calculations were performed at the BLYP level with the standard 6-311 G(df, p) basis set in order to derive the optimized geometry and vibrational wavenumbers of the normal modes because of its accuracy. The computed wavenumbers were scaled by an empirical scaling factor of 0.9986 [15] to fit the experimental wavenumbers; this accounts for systematic errors caused by the incomplete basis set and the fact that electron correlation and vibrational anharmonicity are overlooked. The assignment of the calculated wavenumbers was aided by the VEDA 4 program [16]. The Raman activities (S_i) calculated by Gaussian 03 were converted to relative Raman intensities (I_i) using Eq. 1 (derived from the basic theory of Raman scattering [17]):

$$I_i = \frac{f(\nu_o - \nu_i)^4 S_i}{\nu_i\left[1 - \exp\left(\frac{-hc\nu_i}{kT}\right)\right]}, \quad (1)$$

where ν_o is the exciting wavenumber, ν_i is the vibrational wavenumber of the i^{th} normal mode, h, c, and k are universal constants, and f is a suitably chosen common scaling factor for all peak intensities. The simulated IR and Raman spectra were plotted using pure Lorentzian band shapes with a full width at half maximum (FWHM) of 10 cm^{-1}.

The natural bond orbital (NBO) calculations [18] were done at the DFT level in order to investigate inter- and intramolecular interactions. The hyperconjugative interaction energy was deduced using Eq. 2 based on a second-order perturbation approach [19]:

$$E^{(2)} = -n_\sigma \frac{\langle\sigma|F|\sigma\rangle^2}{\varepsilon_{\sigma^*} - \varepsilon_\sigma} = -n_\sigma \frac{F_{ij}^2}{\Delta E}, \quad (2)$$

where $\langle\sigma|F|\sigma\rangle^2$ or $F^2{}_{ij}$ is the Fock matrix element between the i^{th} and j^{th} NBOs, ε_σ and ε_{σ^*} are the energies of σ and σ^*, and n_σ is the population of the donor σ orbital.

The TD-DFT method was used to calculate the total free energies, the oscillator strength of electronic singlet–singlet transitions, and the absorption wavelengths. The UV-visible absorption spectrum and the solvent effect were investigated using the polarizable continuum model (PCM) [20]. A wide range of solvents were used for the analysis: nonpolar (benzene), slightly polar (chloroform), polar aprotic (acetone, acetonitrile, and dichloromethane), and polar protic (ethanol, methanol, and water). The frontier molecular orbitals and the HOMO–LUMO energy gap were computed.

Results and discussion

Molecular geometries

Optimized bond lengths, bond angles, and dihedral angles of metamitron (I), isometamitron (II) and metribuzin (III) (Fig. 2) calculated using DFT and the corresponding X-ray diffraction (XRD) data [13, 21] are given in Tables 1, 2 and 3. The calculated data for the dimeric forms are very close to the experimental XRD values, and thus the intermolecular hydrogen-bonded dimer structure was found to be more stable. The crystal structure favors additional intermolecular hydrogen bonds and a layered polymeric structure [13].

In the dimer, the molecules are bound together via intermolecular hydrogen-bonded interactions. Due to hydrogen bonding, the C=O bond length increases by 0.012 Å in I and II and by 0.015 Å in III (Table 1). The shortening of the N_{13}–N_{14} / N_{16}–N_{17} / N_2–N_3 bonds (0.017, 0.014, and 0.019 Å in I, II, and III, respectively; Table 1) may be due to the increased double-bond character arising from the delocalization of the electrons in the ring. The six π-electrons required for the aromaticity of the heterocyclic ring come from the two C=N bonds and the unpaired electron present on the nitrogen to which the NH_2 group is attached. If the π-electrons of the C=O bond take part in the delocalization, the system acquires antiaromatic character (eight π-electrons). In order to retain the aromatic character, the polarization of the C=O bond is essential, so the triazinones have polar C^+–O^- bonds rather than C=O bonds. The increased C=O bond length can be attributed to its polar nature, which aids hydrogen-bond formation at the O atom. Full circular delocalization is prevented by the polarized carbonyl group, which contributes no π-electrons to the system, thus breaking the continuity. The resulting distortion of bond character reduces the planarity of the ring, which decreases the aromaticity of the heterocyclic ring. The polar nature of the C=O bond and the resulting reduction in aromaticity were also recently reported for fused ring systems such as benzotriazinones [22]. The electrons from NH_2 are withdrawn by the ring, which reduces the electron density at the N (1.555, 1.542, and 1.591 e in I, II, and III, respectively) of the NH_2 group, which further facilitates the formation of a hydrogen bond between the NH_2 hydrogen and the O atom. The electron

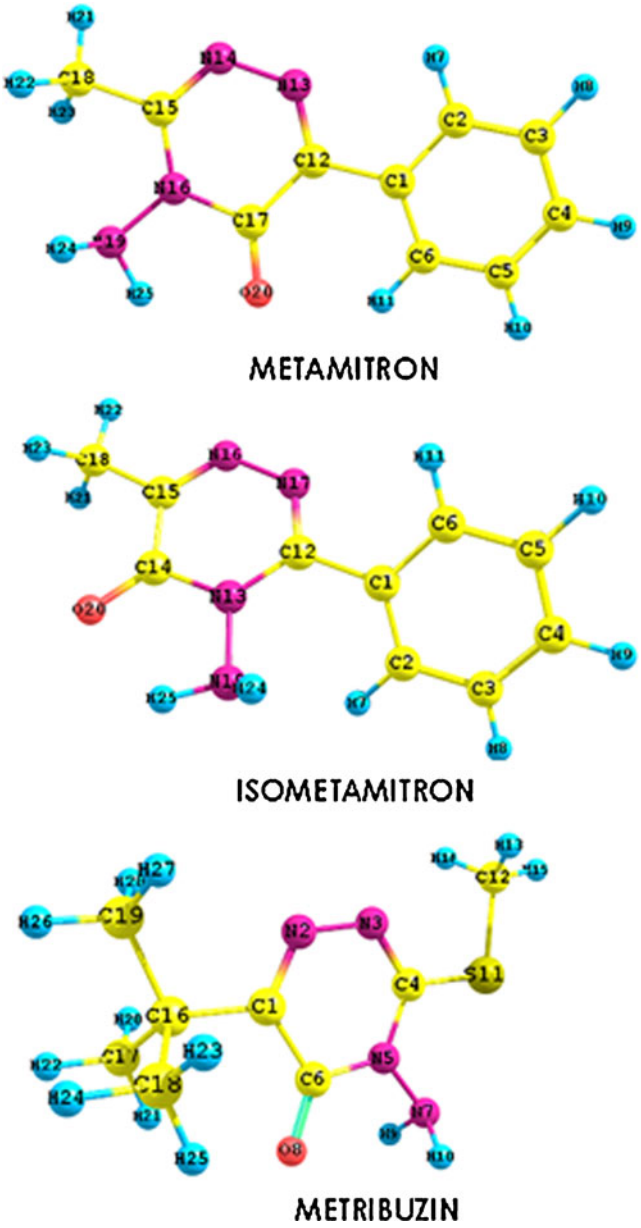

Fig. 2 The optimized structure of the monomer, calculated at the BLYP/6-311 G (df, p) level, showing the atom numbering scheme for triazinone derivatives

flow from the NH_2 group through the azinone heterocyclic ring towards O can produce intramolecular charge transfer (ICT) within the conjugated ring system, which reduces the double-bond character of C=O in all of these molecules and lowers the stretching wavenumber.

DFT calculations for the monomers show a shift in bond angle from 120° at the C_{17} / C_{14} position in I and II. The angle $O_{20}C_{17}N_{16}$ / $O_{20}C_{14}N_{13}$ decreases by 1.6/0.2° (Table 2) and the angle $O_{20}C_{17}C_{12}$ / $O_{20}C_{14}N_{15}$ is enhanced by 9.6/7.3°. Similarly, at C_6 in III, the angle $O_8C_6N_5$ decreases by 0.8° and the angle $O_8C_6C_1$ is enhanced by 8.6°. This asymmetry of the exocyclic angle reveals that there is a change in the hybridization of carbon from sp^2 to sp^3 and that an intramolecular H-bond forms with the hydrogen present in the NH_2 group, so the planarity and delocalization of the π-electrons in the ring decrease.

It was found that the carbon–carbon bond lengths in the benzene ring on the molecular skeleton are intermediate between typical C–C single (1.54 Å) and C=C double (1.34 Å) bonds, and the carbon–nitrogen bond lengths in the heterocyclic ring are also intermediate between typical C–N single (1.47 Å) and C=N double (1.27 Å) bonds, indicating that the π-electrons in the molecules are delocalized. However, due to the asymmetric π-electron cloud, the potential for the carbonyl group to form a hydrogen bond, and the lack of perfect heterocyclic ring planarity, the resonance is reduced. Thus, the aromatic character of the heterocyclic ring decreases, the double bond character of N=C reduces to 1.7, and the N–N single bond character increases to 1.3 for I, instead of the 1.5 expected for a perfect aromatic system [13]. The increases in the C–N and C–C bond distances (C_{17}–N_{16}=1.397 and C_{17}–C_{12}=1.468 Å in I, C_{14}–N_{13}=1.396 and C_{14}–C_{15}=1.456 Å in II, and C_6–N_5=1.398 and C_1–C_6=1.471 Å in III) (Table 1) according to the experimental values clearly show that n→σ* conjugation is occurring between the lone-pair electrons of the O_{20} atom and the C–N and C–C bonds. To increase the aromatic character of the heterocyclic ring (six π-electron system), nonbonded electrons from the nitrogen of the amino group on the ring are utilized for π-bond delocalization, and the π-electrons from the C=O carbon must shift to O; hence C becomes positive (~0.6 e), which is observed for all of the triazinone derivatives studied (Table S1 of the "Electronic supplementary material," ESM). Even though the phenyl ring and methyl group are located at the 3 and 6 positions in I and II, the C=N bond lengths are nearly equal. This means that the influence of the phenyl and methyl substituents on the C=N–N=C group is negligible [13].

Three types of intramolecular and intermolecular H-bonds are possible in the triazinone derivatives: N–H…O, C–H…O, and C–H…N (Tables S2a, S2b, and S2c of the ESM). In compound I, the C_2...N_{13} and N_{19}...O_{20} distances are 2.776 and 2.660 Å, respectively (Table S2a of the ESM); in both cases, this is less than the sum of the related van der Waals radii. The corresponding bond angles C–H–N and N–H–O are 98.3 and 115.3°, respectively, which are both larger than 90° [23], indicating C–H…N and N–H…O intramolecular hydrogen bonding. Similar trends are also observed for compound II. A weak C–H…N intramolecular hydrogen bond is observed along with a strong N–H…O hydrogen bond, with C_2...N_{19} and N_{19}...O_{20} distances of 2.947 and 2.656 Å, respectively (Table S2b of the ESM). The corresponding bond angles for C–H–N and N–H–O are 107.9 and 116.6°, respectively. The decrease in the C_6–H_{11} (1.085 Å) bond length in I shows that an intramolecular C–

Table 1 Optimized bond lengths (Å) of triazinone derivatives, calculated at the BLYP/6-311 G(df, p) level

Metamitron						Isometamitron						Metribuzin					
Parameter	Monomer (m)	Dimer (d)	XRD (e) [a]	Δ(d − m)	Δ(d − e)	Parameter	Monomer (m)	Dimer (d)	XRD (e) [a]	Δ(d − m)	Δ(d − e)	Parameter	Monomer (m)	Dimer (d)	XRD (e) [b]	Δ(d − m)	Δ(d − e)
C12–C1	1.489	1.484	1.485	0.005	0.001	C12–C1	1.492	1.481	1.487	0.011	0.006	C1–C16	1.540	1.531	1.520	0.009	0.011
C12–N13	1.329	1.316	1.307	0.013	0.009	C12–N17	1.327	1.317	1.311	0.010	0.006	C4–N3	1.314	1.308	1.293	0.006	0.015
N13–N14	1.364	1.356	1.373	0.008	0.017	N17–N16	1.371	1.359	1.373	0.012	0.014	N2–N3	1.383	1.366	1.385	0.017	0.019
N14–C15	1.321	1.312	1.308	0.009	0.004	N16–C15	1.319	1.309	1.301	0.010	0.080	N2–C1	1.315	1.308	1.294	0.007	0.014
C15–N16	1.373	1.369	1.358	0.004	0.011	C12–N13	1.381	1.379	1.367	0.002	0.012	C4–N5	1.378	1.372	1.369	0.006	0.003
N16–C17	1.427	1.397	1.385	0.030	0.012	N13–C14	1.424	1.396	1.391	0.028	0.005	C6–N5	1.426	1.398	1.390	0.028	0.008
C17–C12	1.475	1.468	1.464	0.007	0.004	C14–C15	1.461	1.456	1.455	0.001	0.001	C6–C1	1.481	1.471	1.461	0.010	0.010
C15–C18	1.502	1.496	1.489	0.006	0.007	C15–C18	1.504	1.499	1.493	0.005	0.006	–	–	–	–	–	–
N16–N19	1.428	1.417	1.416	0.011	0.001	N13–N19	1.427	1.417	1.416	0.010	0.001	N5–N7	1.426	1.411	1.426	0.015	0.015
C17–O20	1.236	1.237	1.225	0.001	0.012	C14–O20	1.236	1.239	1.227	0.003	0.012	C6–O8	1.231	1.234	1.219	0.003	0.015
C1–C6	1.413	1.404	1.393	0.009	0.011	C1–C2	1.411	1.404	1.394	0.007	0.010	–	–	–	–	–	–
C6–C5	1.399	1.392	1.389	0.007	0.003	C2–C3	1.399	1.393	1.384	0.006	0.009	–	–	–	–	–	–
C5–C4	1.398	1.396	1.374	0.002	0.022	C3–C4	1.400	1.396	1.381	0.004	0.015	–	–	–	–	–	–
C4–C3	1.403	1.396	1.381	0.007	0.015	C4–C5	1.401	1.396	1.374	0.005	0.022	–	–	–	–	–	–
C3–C2	1.394	1.393	1.384	0.001	0.009	C5–C6	1.396	1.392	1.389	0.004	0.003	–	–	–	–	–	–
C2–C1	1.416	1.404	1.394	0.012	0.010	C6–C1	1.411	1.404	1.393	0.007	0.011	–	–	–	–	–	–
C2–H7	1.088	1.084	0.930	0.004	0.154	C2–H7	1.087	1.083	0.930	0.004	0.153	–	–	–	–	–	–
C3–H8	1.091	1.087	0.930	0.004	0.157	C3–H8	1.090	1.086	0.930	0.004	0.156	–	–	–	–	–	–
C4–H9	1.091	1.087	0.930	0.004	0.157	C4–H9	1.090	1.087	0.930	0.003	0.157	–	–	–	–	–	–
C5–H10	1.091	1.087	0.930	0.004	0.157	C5–H10	1.090	1.086	0.930	0.004	0.156	–	–	–	–	–	–
C6–H11	1.085	1.082	0.930	0.003	0.152	C6–H11	1.088	1.084	0.930	0.004	0.157	–	–	–	–	–	–
C18–H21	1.094	1.091	0.960	0.003	0.131	C18–H21	1.101	1.097	0.960	0.004	0.137	–	–	–	–	–	–
C18–H22	1.102	1.095	0.960	0.007	0.135	C18–H22	1.095	1.092	0.960	0.003	0.132	–	–	–	–	–	–
C18–H23	1.099	1.094	0.960	0.005	0.134	C18–H23	1.100	1.096	0.960	0.004	0.136	–	–	–	–	–	–
N19–H24	1.031	1.027	0.960	0.004	.067	N19–H24	1.026	1.022	0.960	0.004	0.062	–	–	–	–	–	–
N19–H25	1.027	1.021	0.928	0.006	0.093	N19–H25	1.032	1.027	0.928	0.005	0.099	–	–	–	–	–	–

[a] From [13]

[b] From [21]

Table 2 Optimized bond angles (°) of triazinone derivatives, calculated at the BLYP/6-311 G(df, p) level

Metamitron						Isometamitron						Metribuzin					
Parameter	Monomer (m)	Dimer (d)	XRD (e) [a]	Δ(d − m)	Δ(d − e)	Parameter	Monomer (m)	Dimer (d)	XRD (e) [a]	Δ(d − m)	Δ(d − e)	Parameter	Monomer (m)	Dimer (d)	XRD (e)[b]	Δ(d − m)	Δ(d − e)
C12–C1–C6	122.9	122.8	122.4	0.1	0.4	C12–C1–C2	123.1	123.1	123.0	0.0	0.1	C18–C16–C1	109.4	109.4	109.7	0.0	0.3
N13–C12–C1	116.8	117.0	117.0	0.2	0.0	N17–C12–C1	116.9	117.1	115.7	0.2	1.4	N2–C1– C16	118.2	118.4	118.0	0.2	0.4
N14–N13–C12	122.6	122.4	121.8	0.2	0.6	N16–N17–C12	120.6	120.5	120.1	0.1	0.4	C6–C1– C16	119.7	120.1	119.6	0.4	0.5
C15–N14–N13	119.5	119.4	118.8	0.1	0.6	Cl5–N16–N17	120.6	120.8	119.9	0.2	0.9	N3–N2–C1	122.3	122.4	121.7	0.1	0.7
C18–C15–N14	119.4	119.1	119.2	0.3	0.1	Cl8–C15–N16	118.8	119.4	118.3	0.6	1.1	C4–N3–N2	118.9	118.9	118.2	0.0	0.7
Nl6–C15–C18	119.1	119.2	118.6	0.1	0.6	Cl4–C15–C18	117.9	118.2	118.3	0.3	−0.1	S11–C4–N3	121.2	121.3	122.1	0.1	0.8
N16–C15–N14	121.5	121.7	122.2	0.2	0.5	Cl4–C15–N16	123.2	122.4	123.4	0.8	1.0	S11–C4–N5	116.2	116.1	114.8	0.1	1.3
Nl9–N16–C15	120.4	118.8	118.6	1.6	0.2	N19–N13–C12	123.3	120.9	122.1	2.4	1.2	N5–C4–N3	122.5	122.5	123.1	0	0.6
Nl9–N16–C17	116.5	118.8	118.7	2.3	0.1	N19–N13–C14	114.9	117.7	116.6	2.8	1.1	N7–N5–C4	118.4	118.1	119.2	0.3	1.1
C17–N16–C15	122.8	122.4	122.6	0.4	0.2	C14–N13–C12	121.7	121.0	121.1	0.7	0.1	N7–N5–C6	119.6	120.2	119.2	0.6	1.0
O20–C17–N16	118.4	119.3	120.1	0.9	0.8	O20–C14–N13	120.1	120.8	120.9	0.7	0.1	C6–N5–C4	121.9	121.7	121.6	0.2	0.1
O20–C17–C12	129.6	127.9	127.1	1.7	0.8	O20–C14–C15	127.3	125.5	125.9	1.8	0.4	O8–C6–N5	119.2	119.6	120.4	0.4	0.8
Cl7–C12–C1	121.7	121.6	121.2	0.1	0.4	N13–C12–C1	121.9	121.5	122.2	0.4	0.7	O8–C6–C1	128.6	127.4	127.1	1.2	0.3
Cl7–C12–N13	121.5	121.3	121.7	0.2	0.4	N13–C12–N17	121.2	121.4	122.1	0.2	0.7	C6–C1–N2	122.1	121.5	122.5	0.6	1.0
Cl2–C1–C2	118.7	118.6	119.2	0.1	0.6	Cl2–C1–C6	117.6	117.5	117.0	0.1	0.5						
Cl–C2–C3	120.8	120.7	120.8	0.1	0.1	Cl–C2–C3	120.1	119.7	119.8	0.4	0.1						
C2–C3–C4	120.4	120.3	120.4	0.1	0.1	C2–C3–C4	120.5	120.4	120.3	0.1	0.1						
C3–C4–C5	119.4	119.5	119.4	0.1	0.1	C3–C4–C5	119.7	119.8	119.9	0.1	0.1						
C4–C5–C6	120.7	120.5	120.8	0.2	0.3	C4–C5–C6	120.2	120.1	120.5	0.1	0.4						
C5–C6–C1	120.4	120.3	120.3	0.1	0.0	C5–C6–C1	120.5	120.4	119.9	0.1	0.5						
C6–C1–C2	118.4	118.6	118.4	0.2	0.2	C6–C1–C2	119.0	119.2	119.7	0.2	0.5						

[a] From [13]

[b] From [21]

H….O hydrogen-bond interaction is also possible. In order to accommodate intramolecular C–H…O hydrogen bonding, the $C_6C_1C_{12}C_{17}$ section of the benzene ring twists (by 11.7°; Table 3), which reduces the extended conjugation of the benzene ring with the heterocyclic ring. An intramolecular C–H…O hydrogen bond is not observed in compound II due to the shifting of the C=O group away from the corresponding hydrogens. Instead, there is strong steric repulsion between H_7 and H_{24}. Hence, the benzene ring is twisted, causing the triazinone ring to be out of plane with respect to the benzene ring, as shown by the dihedral angle $C_2C_1C_{12}N_{13}$ (36.9°) (Table 3). In compound III, intramolecular hydrogen-bond formation occurs with the *t*-butyl group hydrogen (Table S2c of the ESM). In the dimeric form of compound I, the $C_{34}...N_{30}$ and $N_{33}...O_{20}$ distances are 2.423 and 3.007 Å, respectively (Table S2a of the ESM); in both cases, this is less than the sum of the related van der Waals radii. This results in intermolecular C–H…N, C–H…O, and N–H…O hydrogen-bond interactions. Similarly, in II and III, strong intermolecular C–H…N and N–H…O hydrogen-bond interactions are possible (Table S2a of the ESM).

The reduction in planarity and thus the reduction in extended conjugation between the heterocyclic and benzene rings is different for compounds I and II due to changes in hydrogen-bonding character and steric effects. The deviations in the dihedral angles in I are 3.3° for $C_{15}N_{16}C_{17}C_{12}$ and −2.3° for $N_{16}C_{17}C_{12}N_{13}$ (Table 3), and those in II are −2.2° for $C_{15}C_{14}N_{13}C_{12}$ and 3.5° for $C_{14}N_{13}C_{12}N_{17}$. All of the corresponding dihedral angles are 0.0° in III, where there is no possibility of extended conjugation. The energy values calculated by the self-consistent field (SCF) method for the monomeric forms of I, II, and III are −1788608, −1788053, and −2639439 kJ mol^{-1} respectively. The corresponding dimerized energy values are −3577378 (I), −3577350 (II) and −5280719 (III) kJ mol^{-1} (Table S3 of the ESM). The SCF energy of compound III is very different from those of I and II.

Vibrational spectral analysis

The vibrational spectra were analyzed based on the FT-IR and FT-Raman spectra as well as the vibrational wavenumbers computed at the DFT level with the scaled wavenumbers. The observed IR and Raman spectra as well as the simulated theoretical spectra are given in Figs. 3 and 4 for visual comparison. The experimental and the scaled calculated wavenumbers, along with their respective dominant normal modes and the corresponding PEDs (potential energy distributions), are presented in Table 4. The calculated wavenumbers for the monomers and dimers of the three triazinone derivatives, together with their respective assignments, are presented in Table S4 of the ESM. The vibrational analysis is based on the vibrational modes of the phenyl ring, the heterocyclic ring, the carbonyl group, the methyl group, and the amino group.

Vibrations of the amino group

The methyl and amino groups are generally considered electron-donating substituents in aromatic ring systems [24]. A CH_3 group will interact with a nearby π-system via hyperconjugation, while a NH_2 group will share its lone pair of electrons with the π-electrons in the ring. Both mechanisms imply that electronic delocalization can be taken into account by employing the molecular orbital approach. Generally, H-bonding leads to a reduction in the NH_2 stretching wavenumber, an increase in the NH_2 bending wavenumber, and an increase in IR intensity [25]. For primary amines, it is known that asymmetric NH_2 stretching will give rise to a band in the range 3500–3420 cm^{-1}, while symmetric stretching will appear [25] between 3420 and 3280 cm^{-1}. The infrared spectrum shows a medium-intensity band at 3311 cm^{-1} (PED 100%) (Table 4) corresponding to the NH_2 asymmetric stretching mode in I. The observed NH_2 asymmetric stretching wavenumber is lower than may be expected due to the intramolecular N–H…O hydrogen-bond interaction. The corresponding calculated wavenumbers in the monomers of I, II, and III are 3385, 3373, and 3362 cm^{-1} (Table S4 of the ESM). In the dimers, the corresponding calculated wavenumbers are 3367, 3359, and 3377 cm^{-1}, respectively. The intermolecular hydrogen-bonding structures of the triazinone derivative dimers are shown in Fig. 5. Symmetric NH_2 stretching is observed as medium-intensity band in the IR spectrum at 3247 cm^{-1}. The observed NH_2 symmetric stretching wavenumber is lower than might be expected due to the intramolecular N–H…O hydrogen-bond interaction. Ab initio computation indicates that the wavenumbers of these bands for the triazinone monomers (3294, 3245, 3281 cm^{-1}) and the corresponding dimer wavenumbers (3253, 3249, and 3275 cm^{-1}; see Table S4 of the ESM) are redshifted. This redshifting of the N–H stretching wavenumbers is due to the formation of intramolecular and intermolecular N–H…O hydrogen bonding. The redshifting is further enhanced by the reduced N–H bond order values (Table S5 of the ESM), which occurs due to a donor–acceptor interaction. The scissoring mode of the NH_2 group appears in the region 1650–1580 cm^{-1} [25]. In compound I, the observed intense bands in the IR spectrum at 1679 and 1600 cm^{-1} and the corresponding weak and very intense Raman bands at 1662 and 1596 cm^{-1} can be attributed to the scissoring mode of the NH_2 group. The calculated wavenumbers for the NH_2 scissoring mode of monomer I are 1655 and 1608 cm^{-1}, which have very high IR intensities of 63.01 and 192.41 (Table 4), respectively. This

Table 3 Optimized dihedral angles (°) of triazinone derivatives, calculated at the BLYP/6-311 G(df, p) level

Metamitron						Isometamitron						Metribuzin					
Parameter	Monomer (m)	Dimer (d)	XRD (e) [a]	Δ(d − m)	Δ(d − e)	Parameter	Monomer (m)	Dimer (d)	XRD (e) [a]	Δ(d − m)	Δ(d − e)	Parameter	Monomer (m)	Dimer (d)	XRD (e) [b]	Δ(d − m)	Δ(d − e)
N13–C12–C1–C6	−169.1	−159.9	−157.1	9.2	−2.8	N17–C12–C1–C2	−142.3	−140.2	−157.1	2.1	16.9	C18–C16–C1–N2	−120.0	−120.0	−123.3	0	3.3
N13–C12–C1–C2	10.2	18.8	20.3	8.6	−1.5	N17–C12–C1–C6	33.2	35.6	20.3	2.4	15.3	C18–C16–C1–C6	60.0	59.9	55.4	−0.1	4.5
N14–N13–C12–C1	−178.8	−178.8	−179.0	0	0.2	N16–N17–C12–C1	−179.9	−179.9	−179.0	0	−0.9	N2–C1–C16–C19	0.0	−0.2	−4.7	−0.2	4.5
N16–C17–C12–C1	177.1	178.7	178.5	1.6	0.2	C14–N13–C12–C1	−178.2	−176.7	−178.5	1.5	1.8	C6–C1–C16–C19	179.9	179.7	173.9	−0.2	5.8
C17–N16–C15–C18	177.5	177.4	179.5	−0.1	−2.1	N19–N13–C12–C1	−1.1	9.6	−1.8	10.7	11.4	N3–N2–C1–C16	179.9	179.4	177.6	−0.5	1.8
C15–N14–N13–C12	0.3	−0.3	−0.1	−0.6	−0.2	Cl5–N16–N17–C12	−1.3	−3.8	−0.1	−2.5	−3.7	C5–C6–C1–C16	−179.9	−179.5	−173.8	0.4	−5.7
C18–C15–N14–N13	−179.4	−179.4	178.8	0	−358.2	Cl8–C15–N16–N17	−179.2	−178.2	178.8	1	−357	C4–N5–C6–C1	0.0	0.4	−3.6	0.4	4
–	–	–	–	–	–	Cl8–C15–C14–N13	−179.0	−178.5	−179.5	0.5	1	C4–N3–N2–C1	0.0	−0.2	−4.4	−0.2	4.2
Nl6–C15–C18–H23	−52.2	−55.8	−59.9	−3.6	4.1	Cl4–C15–C18–H23	56.46	57.4	−58.9	0.94	116.3	S11–C4–N3–N2	−179.9	−179.1	−175.6	0.8	−3.5
Nl6–C15–C18–H22	67.1	62.8	61.1	−4.3	1.7	Cl4–C15–C18–H22	177.7	178.4	−178.9	0.7	357.3	S11–C4–N5–C6	179.9	178.9	179.7	−1	−0.8
Nl6–C15–C18–H21	−173.5	−176.9	178.0	−3.4	−354.9	Cl4–C15–C18–H21	−61.4	−60.8	61.1	0.6	−121.9	C12–S11–C4–N3	0.0	−0.2	−3.2	−0.2	3
Nl4–C15–C18–H23	128.2	124.6	122.1	−3.6	2.5	Nl6–C15–C18–H23	−121.9	−121.2	122.1	0.7	−243.3	C12–S11–C4–N5	179.9	179.5	175.7	−0.4	3.8
Nl4–C15–C18–H22	−112.5	−116.6	−117.9	−4.1	1.3	Nl6–C15–C18–H22	−0.7	−0.2	2.0	0.5	−2.2	O8–C6–C1–C16	0.0	−0.3	6.3	−0.3	−6.6
Nl4–C15–C18–H21	6.9	3.6	2.04	−3.3	1.56	Nl6–C15–C18–H21	120.3	120.6	−117.9	0.3	238.5	O8–C6–N5–N7	0.0	−178.8	176.3	−178.8	−355.1
N16–C15–N14–N13	0.9	1.1	−0.2	0.2	1.3	Cl4–C15–N16–N17	2.5	3.2	−0.2	0.7	3.4	O8–C6–N5–C4	179.9	−0.7	−15.9	−180.6	15.2
Nl9–N16–C15–N14	−176.6	179.5	−176.9	2..9	2.6	N19–N13–C12–N17	−179.5	−171.0	−176.9	8.5	5.9	O8–C6–C1–N2	−179.9	−179.6	−175.1	0.3	−4.5
Nl9–N16–C17–C12	177.2	179.6	177.8	2.4	1.8	N19–N13–C14–C15	179.5	170.9	177.8	−8.6	−6.9	N5–C4–N3–N2	0.0	1.1	5.6	1.1	−4.5
C17–N16–C15–N14	−2.9	−1.1	−0.5	1.8	−0.6	C14–N13–C12–N17	3.5	2.6	−0.5	−0.9	3.1	N7–N5–C4–N3	−179.9	−179.4	−169.0	0.5	−10.4
C17–N16–N19–H24	109.6	76.7	98.9	−32.9	−22.2	C14–N13–N19–H24	−120.7	−30.7	−12.0	90	−18.7	N7–N5–C6–C1	−179.9	178.6	164.1	−1.3	14.5
C17–N16–N19–H25	−3.8	−34.2	−12.0	−30.4	−22.2	C14–N13–N19–H25	−4.9	80.9	98.9	85.8	−18	C6–N5–C4–N3	0.0	−1.2	−1.5	−1.2	0.3
C15–N16–N19–H24	−76.3	−103.9	−84.5	−27.6	−19.4	C12–N13–N19–H24	62.1	143.1	−84.5	81	227.6	S11–C4–N5–N7	0.0	0.8	0.0	0.8	0.8
C15–N16–N19–H25	170.2	145.2	164.6	−25	−19.4	C12–N13–N19–H25	177.9	−105.3	164.6	−283.2	−269.9	C6–N5–N7–H9	16.1	77.4	83.0	61.3	5.6

Table 3 (continued)

Metamitron						Isometamitron						Metribuzin					
Parameter	Monomer (m)	Dimer (d)	XRD (e) [a]	Δ(d − m)	Δ(d − e)	Parameter	Monomer (m)	Dimer (d)	XRD (e) [a]	Δ(d − m)	Δ(d − e)	Parameter	Monomer (m)	Dimer (d)	XRD (e) [b]	Δ(d − m)	Δ(d − e)
O20–C17–C12–N13	177.6	−179.7	178.1	−357.3	−357.8	O20–C14–C15–N16	177.8	177.2	178.1	−0.6	−0.9	C4–N5–N7–H10	90.7	141.3	109.0	50.6	32.3
O20–C17–N16–C15	−176.4	−179.6	−178.4	−3.2	−1.2	O20–C14–C15–C18	−0.5	−1.3	4.3	−0.8	−5.6	N5–C6–C1–N2	0.0	0.5	4.8	0.5	4.3
O20–C17–C12–C1	−3.2	−1.4	−1.8	1.8	0.4	O20–C14–N13–C12	179.2	179.7	178.1	0.5	1.6						
O20–C17–N16–N19	−2.5	−0.2	−1.9	2.3	1.7	O20–C14–N13–N19	1.9	−6.4	−1.9	−8.3	−4.5						
C17–C12–C1–C6	11.7	21.8	22.81	10.1	−1.01	N13–C12–C1–C2	39.3	38.9	22.81	−0.4	16.09						
C17–C12–C1–C2	−168.9	−159.6	−159.8	9.3	0.2	N13–C12–C1–C6	−145.2	−145.1	−159.8	0.1	14.7						
C12–C1–C2–C3	−179.3	−178.9	−177.2	0.4	−1.7	C12–C1–C2–C3	175.8	176.6	177.3	0.8	−0.7						
C12–C1–C6–C5	179.2	178.6	177.26	−0.6	1.34	C12–C1–C6–C5	−176.8	−177.5	−177.2	−0.7	−0.3						
C12–C1–C2–H7	0.5	0.9	2.7	0.4	−1.8	C12–C1–C2–H7	−3.9	−2.1	−2.7	1.8	0.6						
C12–C1–C6–H11	−1.0	−1.0	2.7	0	−3.7	C12–C1–C6–H11	2.3	2.3	2.7	0	−0.4						
C15–N16–C17–C12	3.3	0.3	1.4	3.0	1.1	C15–C14–N13–C12	−2.2	−2.9	1.4	0.7	1.5						
N16–C17–C12–N13	−2.1	0.5	−1.6	−2.6	−2.1												

[a] From [13]

[b] From [21]

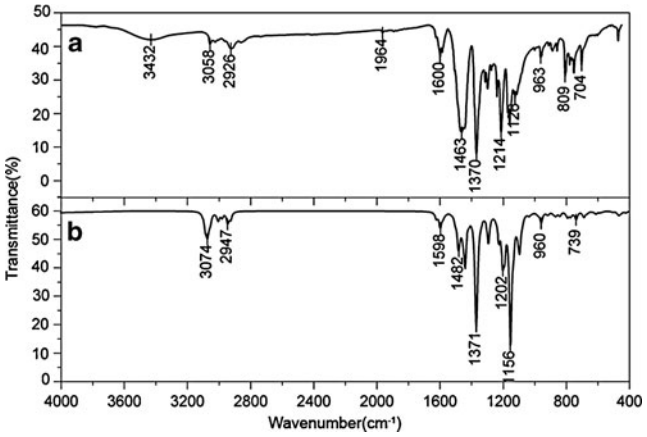

Fig. 3 Combined IR spectrum of metamitron: **a** computed, **b** experimental

intensity enhancement is due to the coupling of this mode with the C=O stretching vibration. This is corroborated by X-ray diffraction studies [13] in crystals. NH_2 wagging will give rise to a band at 800 cm^{-1} [25], while NH_2 wagging is blueshifted and observed as an intense band in the Raman spectrum of I at 999 cm^{-1}. The corresponding calculated values for triazinone monomer derivatives were found to be 992, 1052, and 994 cm^{-1}, which are also blueshifted.

The carbonyl CO vibration

The band associated with the C=O stretching mode was found to be strong and active in both the IR and Raman spectra. This phenomenon is quite unusual, as even in the absence of inversion symmetry, the infrared and Raman spectra are generally complementary: in most cases, the strongest bands in the Raman spectrum are weak in the IR spectrum, and vice versa. However, ICT from the donor to the acceptor group through a conjugated single–double bond path can induce large variations in both the molecular dipole moment and molecular polarizability, making both the IR and Raman activities strong at the same time. Thus, in triazinone derivatives, the simultaneous IR and Raman activation of the C=O stretching mode clearly explains the charge-transfer interaction between the donor and acceptor via the π-conjugated path [26, 27]. The intensity of the C=O stretching band can increase due to conjugation or the formation of hydrogen bonds and depending on the size of the ring to which it is attached [28]. The C=O stretching band is often intense and appears in the region 1680–1670 cm^{-1} [29]. In triazinone derivatives, conjugation of the C=O bond with the heterocyclic aromatic ring may increase its single-bond character, resulting in lowered values for carbonyl stretching wavenumbers. In compound I, the weak and very intense bands in the Raman spectrum at 1662 and 1596 cm^{-1} can be identified as C=O stretching modes. In the IR spectrum, the carbonyl stretching vibration is split into two components that produce intense bands at 1679 and 1600 cm^{-1}. This splitting of the carbonyl mode may be attributed to Fermi resonance and molecular association. The results from the computation indicate that the wavenumbers of these very intense IR modes in the monomer occur at 1655 and 1608 cm^{-1}. The corresponding calculated values for the dimer were found to be 1688 and 1644 cm^{-1}. Similarly, the calculated values for the monomer and dimer in II were (1680, 1600) and (1674, 1564), respectively, while in III they were (1696, 1641) and (1684, 1645 cm^{-1}), respectively (see Table S4 of the ESM).

When a carbonyl is hydrogen bonded, the resonance causes a positive charge to appear on the proton donor atom and a negative charge on the acceptor atom, which tends to encourage the hydrogen bond. The increased association of the proton with the acceptor atom tends to encourage the resonance [C=O…H–X^- ↔ C–O^-…H–X^+]. Thus, hydrogen bonding and resonance are mutually enhanced by the so-called "transfer of allegiance," and they weaken the carbonyl bond and lower C=O stretching wavenumbers [30, 31]. In the present case, the aromaticity factor discussed earlier also enhances the possibility of the conversion of C=O to C^+–O^-, which tends to lower stretching wavenumbers. This mechanism plays an important role in deciding the hydrogen-bonding capabilities of these compounds. The formation of intermolecular hydrogen bonds between these compounds and the proteins in the biological system of interest is the key factor in their herbicidal activities.

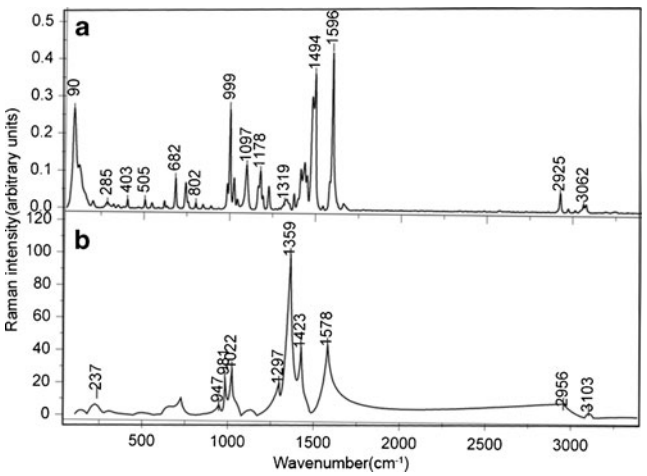

Fig. 4 Combined Raman spectrum of metamitron: **a** computed, **b** experimental

Phenyl ring vibrations

Vibrations of the phenyl ring have been comprehensively studied based on Wilson's numbering convention [32]. The C–H stretching wavenumbers of monosubstituted phenyl

Table 4 Vibrational assignment of metamitron, performed at the DFT level

Observed fundamentals (cm^{-1})			Selective scaled BLYP/6-311G(df, p)		
ν_{IR}	ν_{Raman}	ν_i (cm^{-1})	A_i IR[c]	I_i R[d]	Assignment with PED (%)[e]
3311m		3385	10.25	1.77	$\upsilon_{N19H24asym}$ (79)+$\upsilon_{N19H25asym}$ (21)
3247m		3294	20.09	2.52	$\upsilon_{N19H24sym}$ (21)+$\upsilon_{N19H25sym}$ (78)
3189w		3158	6.07	0.82	$^{2}\ \upsilon_{C6H11}$ (96)
3093w		3131	5.13	1.34	$^{2}\ \upsilon_{C2H7}$ (90)
	3077m	3103	40.24	6.46	$^{20a}\ \upsilon_{C4H9\ ph}$ (53)+$^{20a}\ \upsilon_{C3H8\ ph}$ (19) +$^{20a}\ \upsilon_{C5H10\ ph}$ (24)
3075m		3090	25.12	3.09	$^{20b}\ \upsilon_{C3H8\ ph}$ (49)+$^{20b}\ \upsilon_{C5H10\ ph}$ (49)
	3062m	3079	0.00	1.48	$^{7b}\ \upsilon_{C3H8\ ph}$ (27)+$^{7b}\ \upsilon_{C4H9\ ph}$ (46) +$^{7b}\ \upsilon_{C5H10\ ph}$ (25)
3058vw		3074	3.09	1.77	$\upsilon_{C18H21\ me\ asym}$ (85)+$\upsilon_{C18H23\ me\ asym}$ (12)
3013m		3009	7.57	2.95	$\upsilon_{C18H23\ me\ asym}$ (70)+$\upsilon_{C18H\ 22\ me\ asym}$ (24)
2926m	2925m	2956	16.71	9.8	$\upsilon_{C18H22\ me\ sym}$ (74)+$\upsilon_{C18H23\ me\ sym}$ (17)
1679s	1662w	1655	63.01	1.13	υ_{C20O17} (61)+$\delta_{H25N19H24sci}$ (23)
1600s	1596vs	1608	192.41	0.73	υ_{C20O17} (18)+$\delta_{H25N19H24sci}$ (48)+$\tau_{\ H24N19N16C15}$ (10)+$\tau_{H25N19N16C15}$ (10)
	1581msh	1578	4.67	45.04	$^{8a}\ \upsilon_{C2C3\ ph}$ (32)+$^{8a}\ \upsilon_{C5C4\ ph}$ (12) +$^{8a}\ \upsilon_{C6C5\ ph}$ (10)
1546s	1542vw	1551	1.17	2.04	$^{8b}\ \upsilon_{C5C4\ ph}$ (26)+$^{8b}\ \upsilon_{C4C3\ ph}$ (10) +$^{8b}\ \upsilon_{C1C6\ ph}$ (17)
1492m	1494vs	1482	110.29	0.52	υ_{N14C15} (30)+$\delta_{H23C18H22\ me\ asym}$ (19)+$\delta_{H22C18H21\ me\ asym}$ (10)
1463sbr	1479vs	1477	20.96	3.63	$^{15}\ \delta_{H8C3C4\ ph}$(17)+$^{15}\ \delta_{H10C5C6\ ph}$ (15) +$^{15}\ \delta_{H11C6C5\ ph}$ (19)
	1448m	1443	1.23	17.85	$^{18a}\ \delta_{H9C4C5\ ph}$(19)+$^{18a}\ \delta_{H10C5C6\ ph}$ (11)
1432s	1434m	1437	16.39	6.58	$\delta_{H21C18H23\ me\ asym}$ (23)+$\delta_{H22C18H21\ me\ asym}$ (43)+$\tau_{H21C18N15C16}$ (14)
1417vw	1413m	1423	32.26	43.61	$\delta_{H24N19N16}$ (19)
	1396vw	1410	64.08	6.81	υ_{N14C15} (11)+υ_{N13C12} (15)+$\delta_{H21C18H23\ me\ asym}$ (10)+$\delta_{H23C18H22\ me\ asym}$ (28)
1370vs	1373m	1371	2.55	13.58	$\delta_{H21C18H23\ me\ sym}$ (30)+$\delta_{H23C18H22\ me\ sym}$ (12)+$\delta_{H22C18H21\ me\ sym}$ (18)
	1344w	1359	2.36	100.	υ_{N13C12} (29)
1334s	1334mbr	1325	11.67	8.38	$^{3}\ \delta_{H7C2C3\ ph}$ (25)+$^{3}\ \delta_{H11C6C5\ ph}$ (22)
1302m	1319vw	1300	23.75	3.26	$^{14}\ \upsilon_{C2C3\ ph}$ (10)+$^{14}\ \upsilon_{C4C3\ ph}$ (11) +$^{14}\ \upsilon_{C6C5\ ph}$ (14)+$^{14}\ \upsilon_{C1C6\ ph}$ (18)
	1288vw	1297	7.70	21.44	$\delta_{H24N19N16}$ (46)
1268vw		1260	79.21	2.42	υ_{N13C12} (15)+υ_{C12C1} (16)
1214s	1226m	1183	9.73	1.82	$^{9a}\ \upsilon_{C6C5\ ph}$ (14)
1173s	1178m	1171	12.25	0.62	υ_{N19N16} (19)
	1164msh	1156	0.63	1.34	$^{18b}\ \delta_{H8C3C4\ ph}$ (23) +$^{18b}\ \delta_{H9C4C5\ ph}$ (35)
		1144	21.09	8.21	υ_{N14N13} (20)+υ_{C12C1} (10)
1094s	1097m	1077	6.39	0.48	$^{14}\ \upsilon_{C2C3\ ph}$ (13)+$^{14}\ \upsilon_{C6C5\ ph}$ (15)
	1043w	1034	42.18	16.68	υ_{N14N13} (15)
		1029	1.71	2.56	$\tau_{H21C18C15N16}$ (17)+$\tau_{H23C18C15N16}$ (20)
1024s	1024m	1022	45.22	30.08	υ_{N16C17} (12)
1011vw		1003	18.14	1.02	υ_{N16C17} (10)+$^{12}\ \delta_{C2C3C4\ ph}$ (10)+$\tau_{H22C18C15N16}$ (11)
	999s	992	57.51	7.57	$^{12}\ \delta_{C2C3C4\ ph}$ (17)+$\tau_{H24N19N16C15}$ (10)+$\tau_{H25N19N16C15}$ (10)
986w	984mbr	981	59.88	24.17	υ_{N14N13} (11)
		979	0.35	0.18	$^{17a}\ \gamma_{H7C2C3C4\ ph}$ (14)+$^{17a}\ \gamma_{H8C3C2C1\ ph}$(21)+$^{17a}\ \gamma_{H9C4C3C2\ p\ h}$ (10)+$\tau_{C2C3C4C5\ ph}$ (16)+$\tau_{C6C5C4C3\ ph}$ (11)+$\tau_{C1C6C5C4\ ph}$ (12)
963w		960	3.11	0.09	$^{17a}\ \gamma_{H7C2C3C4\ ph}$(19)+$^{17a}\ \gamma_{H10C5C6C1\ ph}$(23)+$^{17a}\ \gamma_{H11C6C1C12\ ph}$ (29)+$\tau_{C1C6C5C4\ ph}$(15)
931 m		947	5.74	7.12	υ_{N16C17}(19)+$\delta_{C15N14N13}$ (10)
		924	2.30	0.13	$^{17a}\ \gamma_{H7C2C3C4\ ph}$(18)+$^{17a}\ \gamma_{H9C4C3C2\ ph}$(37)+$^{17a}\ \gamma_{H11C6C1C12\ ph}$ (31)+$\tau_{C1C6C5C4\ ph}$ (15)
890vs	891vw	851	38.65	1.78	$\delta_{C5C4C3\ Ph}$ (11)
846vw	843w	839	0.40	0.8	$^{10a}\ \gamma_{H8C3C2C1ph}$ (31)+$^{10a}\ \gamma_{H10C5C6C1ph}$ (25)+$^{10a}\ \gamma_{H11C6C1C12\ ph}$ (21)
809vs	802w	780	17.94	0.13	$^{10b}\ \gamma_{\ H8C3C2C1\ ph}$ (11)+$^{10b}\ \gamma_{\ H9C4C3C2\ ph}$ (12)+$^{10b}\ \gamma_{\ H10C5C6C1\ ph}$ (14)+$\tau_{C15N14N13C12}$

Table 4 (continued)

Observed fundamentals (cm^{-1})			Selective scaled BLYP/6-311G(df, p)		
ν_{IR}	ν_{Raman}	ν_i (cm^{-1})	A_i IR[c]	I_i R[d]	Assignment with PED (%)[e]
					(10)+$\tau_{O20N16C12C17}$ (24)+$\tau_{C12C6C2C1\ ph}$ (14)
755vs	758wsh	739	6.60	0.41	$\tau_{O20N16C12C17}$(29)+$^{11}\ \gamma\ \tau_{H8C3C2C1}$ (10)
	742m	725	0.89	11.24	υ_{C18C15} (20)+$\delta_{C15N14N13}$ (17) +$^{6b}\delta_{C5C4C3\ Ph}$ (18)
704m	682m	688	38.91	0.33	$\tau_{C1C6C5C4\ ph}$ (31)+$^{11}\ \gamma\ _{H9C4C3C2\ ph}$ (23)
677ssh		659	22.19	9.97	υ_{N16C15} (16)+$\delta_{N16C15N14}$ (10)
630vs		619	0.65	1.96	$^{6b}\delta_{C2C3C4\ ph}$ (20)+$^{6b}\delta_{C6C5C4\ ph}$ (37)
	618w	612	3.43	0.22	$\tau_{C18N16N14C15}$ (24)
603vw		611	8.94	0.96	υ_{N16C15} (23)+$\delta_{N19N16C17}$ (13)
544s	545vw	570	0.21	0.28	υ_{C18C15} (13)+$\delta_{O20C17C12}$ (13)
508m	505w	538	19.81	1.22	$\tau_{C15N14N13C12}$ (20)+$\tau_{O20N16C12C17}$ (19)+$\tau_{C12C6C2C1}$ (19)
490vw		486	2.36	2.91	υ_{N19N16} (11)+$\delta_{C15N14N14}$ (10)+$\delta_{N16C15N14}$ (14)
462w		450	1.55	0.1	$\tau_{C15N14N13C12}$ (27)+$^{16b}\gamma_{\ C6C5C4C4\ ph}$ (10)+$\tau_{C17N16C15N14}$ (13)+$\tau_{N19C15C17N16}$ (20)
407w	403w	399	1.40	0.82	$^{16b}\gamma_{\ C2C3C4C5\ ph}$(31)+$^{16b}\ \gamma_{\ C6C5C4C3\ ph}$ (19)
		391	17.82	0.65	$\delta_{O20C17C12}$ (24)+$\delta_{N19N16C17}$ (39)
	349w	349	0.24	1.3	$\tau_{N14N13C12C1}$ (18)+$\tau_{C18N16N14C15}$ (14)
	322w	325	0.25	1.75	$\delta_{C12C1C2}$ (12)
		310	3.07	3.55	$\delta_{C18C15N14}$ (50)
	285w	281	1.07	1.5	υ_{C12C1} (24)
		249	4.74	0.77	$\tau_{N19C15C17N16}$ (50)+$\tau_{C18N16N14C15}$ (14)
		237	54.08	13.81	$\tau_{H24N19N16C15}$ (24)+$\tau_{H25N19N16C15}$ (33)+$\tau_{N19C15C17N16}$ (15)
	202vw	180	0.99	0.52	$\tau_{H22C18C15N16}$ (23)+$\tau_{H23C18C15N16}$ (19)+$\tau_{H21C18C15N16}$ (20)
	156wsh	160	1.66	2.97	$\tau_{N16C15N14N13}$ (14)
	121msh	135	1.30	4.39	$\tau_{C12C6C2C1}$ (10)+$\delta_{C12C1C2}$ (15)
	90s	109	0.60	0.58	$\tau_{C17N16C15N14}$ (53)+$\tau_{C15N14N13C12}$ (12)
		51	5.15	1.79	$\tau_{N14N13C12C1}$ (45)+$\tau_{N16C15N14N13}$ (26)
		20	0.26	56.61	$\tau_{N13C12C1C6}$ (90)

vvs very very strong, *vs* very strong, *s* strong, *m* medium intensity, *sh* shoulder, *w* weak, *vw* very weak, *br* broad, *ph* phenyl ring; *me* methyl, υ stretching, δ in-plane bending, γ out-of-plane bending, τ torsion, *sci* scissoring, *sym* symmetric, *asym* asymmetric

[c] Calculated IR intensities, [d] relative Raman intensities, normalized to 100; cf. Eq. 3, [e] only PED values greater than 10% are given

rings are expected [32] to occur in the region 3120–3010 cm^{-1}. The normal vibrations 2, 7a, 7b, 20a, and 20b are classified as C–H stretching vibrations. The weak band in the IR spectrum at 3189 cm^{-1} corresponds to mode 2, with a PED value of 96% (Table 4). Due to weak hydrogen bonding, there is blueshifting (69 cm^{-1}) in the C_6–H_{11} stretching wavenumber. This blueshifting was also seen in the computed wavenumbers for the monomers and dimers of I and II (Table S4 of the ESM). Mode 20b is IR active and is observed as a medium-intensity band at 3075 cm^{-1}. In the Raman spectrum, 20a is observed as a medium-intensity band at 3077 cm^{-1}. The normal mode 7b appears as medium-intensity band in the Raman spectrum at 3062 cm^{-1}, while the corresponding calculated value for the monomer is 3079 cm^{-1}. Most of the C–H stretching modes were found to be weak, due to the charge transfer from the hydrogen atom to the carbon atom. The selection rule for a monosubstituted benzene ring allows five C–C stretching modes: 8a, 8b, 19a, 19b, and 14. Vibrational mode 8a is redshifted in the Raman spectrum, giving a medium shoulder intensity at 1581 cm^{-1}. The redshifting of the C–C stretching mode 8a clearly indicates a high degree of hyperconjugation in the side chain. DFT computation shows this mode at 1578 cm^{-1}. The strong band observed at 1546 cm^{-1} (Table 4) in the IR spectrum was identified as the 8b mode. Simultaneous activation of the 8a and 8b modes clearly points to intramolecular charge transfer (ICT), which leads to the enhanced herbicidal activity of the compound. Mode 14 is expected [32] to occur in the range 1350–1300 cm^{-1}. The medium-intensity band in the IR spectrum at 1302 cm^{-1} correlates with mode 14. The normal vibrations 3, 9a, 15, 18a, and 18b are categorized as

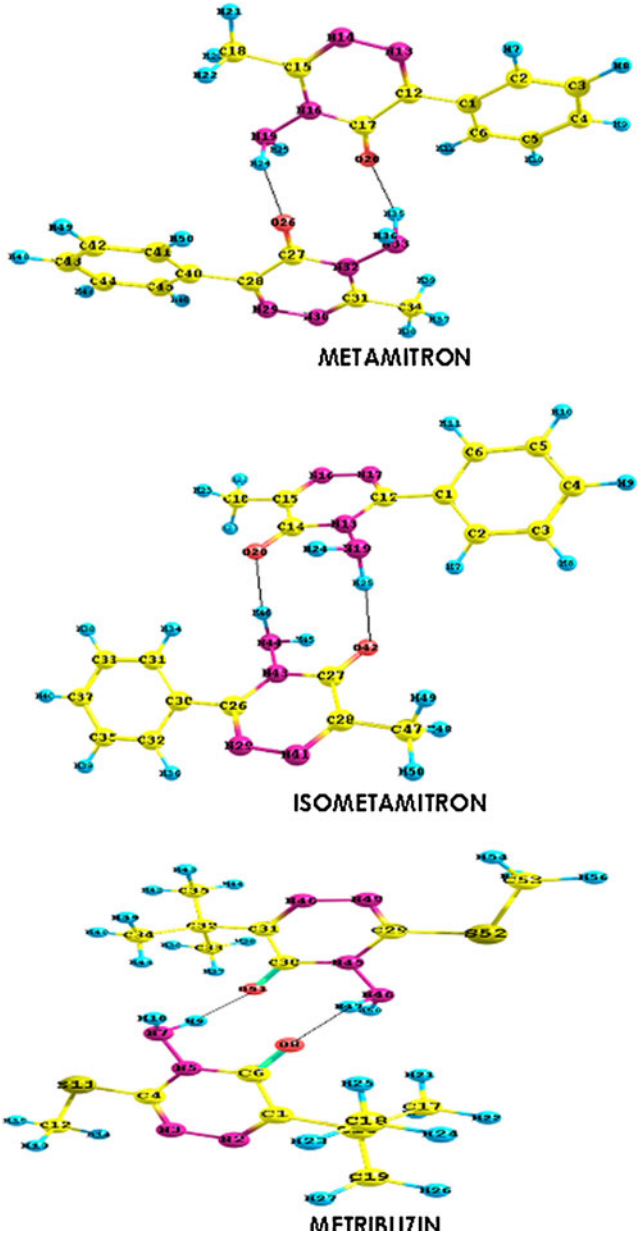

Fig. 5 Dimerized triazinone derivatives, showing the intermolecular hydrogen bonding

C–H in-plane bending vibrations. Mode 3 appears as a strong band in the IR and a broad medium-intensity band in the Raman spectrum at 1334 cm^{-1}. Mode 9a was observed as a strong band in the IR spectrum at 1214 cm^{-1} and a medium-intensity band in the Raman spectrum at 1226 cm^{-1}. The IR band observed at 1164 cm^{-1} was assigned to the 18b mode. The corresponding calculated value lies at 1156 cm^{-1}. The C–H out-of-plane bending vibrations 5, 10a, 10b, 11, and 17a are possible in a monosubstituted benzene ring. The wavenumbers 846 and 809 cm^{-1} in the IR spectrum correspond to modes 10a and 10b. Their counterparts in the Raman spectrum are observed at 843 and 802 cm^{-1}.

Methyl group vibration

The position of the band due to CH_3 group vibration is dependent almost entirely on the nature of the element to which the methyl group is attached. The asymmetric C–H stretching mode is expected to occur around 2980 cm^{-1} and the symmetric stretching is expected at 2870 cm^{-1} [27, 28]. The asymmetric stretching in I is observed as a weak band in the IR spectrum at 3058 cm^{-1}. The corresponding calculated values for I and II are 3074 and 3078 (monomer) and 3059 and 3046 cm^{-1} (dimer), respectively (Table S4 of the ESM). The symmetric stretching mode is observed as a medium band in the IR and Raman spectra at 2925 cm^{-1}. The decrease in intensity and the blueshift of the methyl stretching are due to the electron-donating inductive effect and the rehybridization effect of the methyl group attached to the heterocyclic ring. These effects can be taken into account using a molecular orbital approach, which can highlight changes in polarizability and dipole moment due to electron delocalization [33].

The asymmetric C–H deformation mode of the methyl group is observed in the IR spectrum at 1432 and 1492 cm^{-1} and the Raman spectrum at 1434 and 1494 cm^{-1} (Table 4), and these values are extremely stable since the methyl group is attached to another carbon atom. The symmetric bending vibrations normally appear [28] in the region 1390–1370 cm^{-1}. The medium-intensity band observed at 1373 cm^{-1} in the Raman spectrum and the very intense band at 1370 cm^{-1} in the IR spectrum are due to symmetric bending.

Heterocyclic ring vibrations

Performing calculations for isolated molecules yields only a reasonable model for the heterocyclic ring that can provide acceptable agreement between the observed and calculated spectral profiles. Heterocyclic C=N stretching vibrations are observed in the Raman spectrum of I at 1494, 1396, and 1344 cm^{-1}, and its counterpart in the IR spectrum is observed as a medium-intensity band at 1492 cm^{-1}, as expected [34]. The heterocyclic ring C=N stretch is usually coupled with bending modes. The corresponding calculated values for monomer I are 1482 (very intense), 1410, and 1359 cm^{-1} (Table 4 and Table S4 of the ESM). The N–N stretching vibration generally appears [35] in the range 1035–1029 cm^{-1}. In I, the N–N stretching band in the Raman spectrum is observed at 1178 and 1043 cm^{-1}, and the IR band is found at 1173 cm^{-1} (Table 4). The corresponding calculated values lie at 1171 and 1034 cm^{-1} for the monomer of I. The medium-intensity IR band observed at 931 cm^{-1} and the corresponding calculated wavenumber at 947 cm^{-1} explicitly correlate with the in-plane C–N–N bending mode.

NBO analysis

NBO analysis provides a description of the structure of a compound based on a set of localized bond, antibond, and Rydberg extravalence orbitals that can be used to identify and confirm possible intra- and intermolecular interactions between the units that would lead to proper and improper hydrogen bonding. Some electron donor and acceptor orbitals and stabilization energies resulting from second-order microdisturbance theory have been reported [36]. In order to investigate the various second-order interactions between the filled orbitals of one subsystem and the vacant

Table 5 Second-order perturbation theory analysis of the Fock matrix in the NBO basis for monomers and dimers of triazinone derivatives

Compounds	Nature	Donor NBO (*i*)	ED(*i*) (e)	Acceptor NBO (*j*)	ED(*j*) (e)	$E^{(2)}$ (kJ/mol)
Metamitron	Monomer	π (C_1–C_6)	1.631	π^* (C_2–C_3)	0.289	82.1
				π^* (C_4–C_5)	0.323	78.8
				π^* (C_{12}–N_{13})	0.265	83.2
		π (C_2–C_3)	1.670	π^* (C_1–C_6)	0.369	76.3
				π^* (C_4–C_5)	0.323	87.8
		π (C_4–C_5)	1.660	π^* (C_1–C_6)	0.369	89.7
				π^* (C_2–C_3)	0.289	76.2
		n_1(N_{13})	1.932	σ^* (C_{17}–O_{20})	0.010	2.5
	Dimer	π (C_1–C_6)	1.642	π^* (C_2–C_3)	0.303	84.6
				π^* (C_4–C_5)	0.327	81.5
				π^* (C_{12}–N_{13})	0.219	54.8
		π (C_2–C_3)	1.663	π^* (C_1–N_6)	0.364	81.8
				π^* (C_4–C_5)	0.327	89.3
		π (C_4–C_5)	1.658	π^* (C_1–C_6)	0.364	90.0
				π^* (C_2–C_3)	0.303	79.8
		n_1(N_{13})	1.930	σ^* (C_{17}–O_{20})	0.010	2.5
Isometametron	Monomer	π (C_1–C_2)	1.647	π^* (C_3–C_4)	0.325	77.6
				π^* (C_5–C_6)	0.299	83.5
				π^* (C_{12}–N_{17})	0.322	63.0
		π (C_3–C_4)	1.649	π^* (C_1–C_2)	0.375	93.4
				π^* (C_5–C_6)	0.299	77.3
		π (C_5–C_6)	1.654	π^* (C_1–C_2)	0.375	79.0
				π^* (C_3–C_4)	0.325	89.2
		n_1(N_{16})	1.937	σ^* (C_{14}–O_{20})	0.010	2.1
		n_1(N_{13})	1.542	π^* (C_{14}–H_{20})	0.377	215.9
	Dimer	π (C_1–C_2)	1.638	π^* (C_3–C_4)	0.327	78.7
				π^* (C_5–C_6)	0.302	84.4
				π^* (C_{12}–N_{17})	0.307	61.0
		π (C_3–C_4)	1.647	π^* (C_1–C_2)	0.373	93.4
				π^* (C_5–C_6)	0.302	77.3
		π (C_5–C_6)	1.654	π^* (C_1–C_2)	0.373	79.5
				π^* (C_3–C_4)	0.327	89.7
		n_1(N_{16})	1.937	σ^* (C_{14}–O_{20})	0.020	2.1
Metribuzin	Monomer	n_1(N_2)	1.927	σ^* (C_6–O_8)	0.010	2.5
		n_1(N_5)	1.591	π^* (C_6–O_8)	0.318	224.7
	Dimer	n_1(N_5)	1.555	π^* (C_6–O_8)	0.382	232.6
		n_1(N_7)	1.943	σ^* (C_{30}–O_{51})	0.020	0.3
		n_1(N_{46})	1.942	σ^* (C_6–O_8)	0.010	0.2
		n_1(N_2)	1.931	σ^* (C_6–O_8)	0.010	2.5

ED electron density

$E^{(2)}$ energy of hyperconjugative interactions (stabilization energy)

orbitals of another subsystem, DFT-level calculations have been used, and these predict the delocalization [37]. A large number of stabilizing orbital interactions are observed in the monomers and dimers of the triazinone derivatives, most of them between vicinal NBOs and a few between geminal or remote orbitals. A large $E^{(2)}$ value indicates a relatively intense interaction between the electron donor and acceptor. Intramolecular hyperconjugative interactions are formed through orbital overlap between π (C–C) and π* (C–C) bond orbitals, which results in an intramolecular charge transfer (ICT), stabilizing the system. In the monomers of I and II, the stabilization energy contributions from the π (C_1–C_6) / π (C_2–C_3)→π* (C_4–C_5) interactions are 78.8 and 87.8 kJ mol^{-1} (I), and those from the π (C_1–C_2) / π (C_5–C_6)→π* (C_3–C_4) interactions are 77.6 and 89.2 kJ mol^{-1} (II). Similarly, for the dimers, the corresponding values for I are 81.5 and 89.3 kJ mol^{-1} and for II are 78.7 and 89.7 kJ mol^{-1} (Table 5). There is therefore an increase in stabilization energy when the molecule is in the dimeric form.

The interactions result in a loss of occupancy from the localized NBO of the idealized Lewis structure into an empty non-Lewis orbital, as presented in Tables 5, 6 and 7. There has been considerable interest in the various types of intramolecular and intermolecular interactions. This is understandable, as these interactions play an important role in crystal engineering, molecular recognition, and conformational equilibria. A number of C–H…O, C–H…N, and N–H…O [38–42] complexes have been investigated, and one of the most interesting characteristics observed is the redshift of the wavenumber of the N–H stretching vibration and the blueshift of the C–H stretching vibration.

In the present study, the intramolecular N–H…O hydrogen bond is exposed in the NBO analysis results (Tables 6, 7) as being due to the interaction between the oxygen lone pair and the N–H antibonding orbital n_1 (O_{20})→σ* (N_{19}–H_{25}) and n_2 (O_{20})→σ* (N_{19}–H_{25}). In spite of the fact that the energetic contributions [2.6 : 8.9 (I) and 5.2 : 19.7 (II) kJ mol^{-1}] of the hyperconjugative interactions in the mononmers are weak, these $E^{(2)}$ values are chemically significant and can be used as a measure of the intramolecular delocalization. The weakening and elongation of N–H bonds occur due to hyperconjugation. The redshift of the N–H stretching wavenumber is revealed by the high value of the electron density [0.019 (I): 0.027 e (II)] in the σ* N–H orbital. The NBO results, optimized geometrical parameters, and corresponding downshift in the N–H stretching wavenumber predict the redshift caused by hydrogen bonding. The existence of intramolecular C–H…O hydrogen bonds due to the interaction of the lone pair of oxygen n_1 (O_{20}) and n_2 (O_{20}) with the antibonding orbital σ* (C_6–H_{11}) is confirmed by the results of NBO analysis for the monomers of I and III. The strengthening and contraction of the C–H bonds are due to rehybridization; a blueshift in the C–H stretching wavenumber is indicated by the low values of electron density (0.018 and 0.009 e) along with stabilization energies of 6.2 and 9.7 (I) and 2.8 (III) kJ mol^{-1} for the σ* (C_6–H_{11}) / σ* (C_{17}–H_{21}) orbital. The decrease in ED occurred as a consequence of the formation of a new mesomeric state.

The calculations for the dimers of compounds II and III indicate C–H…O hydrogen bonding, as shown by the interactions n_1 (O_{20})→σ* (C_{31}–H_{34}) and n_2 (O_8)→σ* (C_{18}–H_{25}) that have stabilization energies of 0.3 and 2.7 kJ mol^{-1} and low ED values (0.012 and 0.009 e). The dominant rehybridization effect leads to a shortening of the C–H bond and a blueshift in its stretching vibrational wavenumber. NBO analysis of the dimers of I and II clearly reveals the formation of strong intermolecular N–H…O hydrogen bonding, leading to elongation and a concomitant redshift in the N–H stretching wavenumber. The strong intermolecular H-bonding explains the stability of the dimeric forms of the triazinone derivatives over the monomers, and the increased herbicidal activities of these compounds.

Table 6 Second-order perturbation theory analysis of the Fock matrix in the NBO basis corresponding to the intramolecular and intermolecular N–H...O, C–H...O, and C–H…N hydrogen bonds in the monomers of the triazinone derivatives ($E^{(2)}$, in kJ mol^{-1}), along with hybrid orbitals (HO) and electron density (ED)

Metamitron					Isometamitron					Metribuzin		
Donor NBO (i)	Acceptor NBO (j)	$E^{(2)}$	HO	ED (e)	Donor NBO (i)	Acceptor NBO (j)	$E^{(2)}$	HO	ED (e)	Donor NBO (i)	Acceptor NBO (j)	$E^{(2)}$
$n_1(O_{20})$	σ* (N_{19}–H_{25})	2.6	$Nsp^{2.74}$	0.019	$n_1(O_{20})$	σ* (N_{19}–H_{25})	5.2	$Nsp^{2.65}$	0.027	$n_2(O_8)$	σ* (C_{17}–H_{21})	2.8
$n_1(O_{20})$	σ* (C_6–H_{11})	6.2	$Csp^{2.26}$	0.018	$n_2(O_{20})$	σ* (N_{19}–H_{25})	19.7	$Nsp^{2.65}$	0.027	$n_2(O_8)$	σ* (C_{18}–H_{25})	2.8
$n_2(O_{20})$	σ* (C_6–H_{11})	9.7	$Csp^{2.26}$	0.018	$n_1(N_{19})$	σ* (C_2–H_7)	6.3	$Csp^{2.29}$	0.014	$n_1(N_2)$	σ* (C_{19}–H_{26})	3.2
$n_2(O_{20})$	σ* (N_{19}–H_{25})	8.9	$Nsp^{2.74}$	0.019	$n_1(N_{16})$	σ* (C_{18}–H_{22})	2.1	$Csp^{3.02}$	0.005	$n_1(N_3)$	σ* (C_{12}–H_{15})	2.5
$n_1(N_{13})$	σ* (C_2–H_7)	4.4	$Csp^{2.31}$	0.015	$n_1(N_{16})$	σ* (C_{14}–O_{20})	2.1	$Csp^{2.02}$	0.010	$n_1(N_2)$	σ* (C_6–O_8)	2.5
$n_1(N_{14})$	σ* (C_{18}–H_{21})	2.6	$Csp^{3.00}$	0.006	$n_1(N_{13})$	π* (C_{14}–H_{20})	215.9	$Csp^{99.9}$	0.377	$n_1(N_5)$	π* (C_6–O_8)	224.7
$n_1(N_{13})$	σ* (C_{17}–O_{20})	2.5	$Csp^{2.02}$	0.010								

Table 7 Second order perturbation theory analysis of the Fock matrix in the NBO basis corresponding to the intramolecular and intermolecular N–H...O, C–H...O, and C–H...N hydrogen bonds in the dimers of the triazinone derivatives ($E^{(2)}$, in kJ mol^{-1}), along with hybrid orbitals (HO) and electron density (ED)

Metamitron					Isometamitron					Metribuzin				
Donor NBO (i)	Acceptor NBO (j)	$E^{(2)}$	HO	ED (e)	Donor NBO (i)	Acceptor NBO (j)	$E^{(2)}$	HO	ED (e)	Donor NBO (i)	Acceptor NBO (j)	$E^{(2)}$	HO	ED (e)
$n_1(N_{14})$	$\sigma^*(C_{18}–H_{21})$	2.6	$Csp^{2.99}$	0.006	$n_1(N_{16})$	$\sigma^*(C_{18}–H_{22})$	2.1	$Csp^{3.02}$	0.006	$n_1(N_2)$	$\sigma^*(C_{19}–H_{26})$	3.3	$Csp^{3.24}$	0.007
$n_1(N_{19})$	$\sigma^*(C_{18}–H_{21})$	4.0	$Csp^{2.99}$	0.006	$n_1(N_{41})$	$\sigma^*(C_{47}–H_{50})$	2.1	$Nsp^{3.02}$	0.006	$n_1(N_3)$	$\sigma^*(C_{12}–H_{15})$	2.5	$Csp^{2.97}$	0.006
$n_1(O_{20})$	$\sigma^*(N_{33}–H_{35})$	11.3	$Nsp^{2.51}$	0.022	$n_1(O_{20})$	$\sigma^*(C_{31}–H_{34})$	0.3	$Csp^{2.34}$	0.012	$n_1(N_5)$	$\sigma^*(N_7–H_9)$	11.8	$Nsp^{2.54}$	0.040
$n_2(O_{20})$	$\sigma^*(N_{33}–H_{35})$	1.8	$Nsp^{2.51}$	0.022	$n_1(O_{20})$	$\sigma^*(N_{44}–H_{46})$	23.3	$Nsp^{2.68}$	0.033	$n_1(N_5)$	$\sigma^*(N_7–H_{10})$	10.8	$Nsp^{2.88}$	0.013
$n_1(O_{26})$	$\sigma^*(N_{19}–H_{24})$	11.3	$Nsp^{2.51}$	0.022	$n_2(O_{20})$	$\sigma^*(N_{44}–H_{46})$	3.0	$Nsp^{2.68}$	0.033	$n_2(O_8)$	$\sigma^*(C_{17}–H_{21})$	2.7	$Nsp^{3.05}$	0.009
$n_2(O_{26})$	$\sigma^*(N_{19}–H_{24})$	1.8	$Nsp^{2.51}$	0.022	$n_2(O_{20})$	$\sigma^*(N_{19}–H_{24})$	4.0	$Nsp^{2.87}$	0.015	$n_2(O_8)$	$\sigma^*(C_{18}–H_{25})$	2.7	$Nsp^{3.03}$	0.009
$n_1(N_{30})$	$\sigma^*(C_{34}–H_{38})$	2.6	$Csp^{2.99}$	0.006	$n_1(O_{42})$	$\sigma^*(C_2–H_7)$	0.3	$Nsp^{2.34}$	0.012	$n_1(O_{32})$	$\sigma^*(N_7–H_9)$	27.4	$Nsp^{2.54}$	0.040
$n_1(N_{33})$	$\sigma^*(C_{34}–H_{38})$	4.0	$Csp^{2.99}$	0.006	$n_1(O_{42})$	$\sigma^*(N_{19}–H_{25})$	23.2	$Nsp^{2.68}$	0.033	$n_2(O_{32})$	$\sigma^*(N_7–H_9)$	2.1	$Nsp^{2.54}$	0.040
$n_1(N_{13})$	$\sigma^*(C_{17}–O_{21})$	2.5	$Csp^{2.04}$	0.010	$n_2(O_{42})$	$\sigma^*(N_{19}–H_{25})$	3.1	$Nsp^{2.68}$	0.033	$n_1(N_2)$	$\sigma^*(C_6–O_8)$	2.5	$Csp^{2.07}$	0.010
					$n_2(O_{42})$	$\sigma^*(N_{44}–H_{45})$	4.0	$Nsp^{2.87}$	0.015	$n_1(N_5)$	$\pi^*(C_6–O_8)$	232.6	$Csp^{99.99}$	0.380
					$n_1(N_{16})$	$\sigma^*(C_{14}–O_{20})$	2.1	$Csp^{2.07}$	0.020	$n_1(N_7)$	$\sigma^*(C_{30}–O_{51})$	0.3	$Csp^{2.05}$	0.020
										$n_1(N_{46})$	$\sigma^*(C_6–O_8)$	0.2	$Csp^{2.07}$	0.010

Electronic absorption spectra

The computed electronic spectra of I and II in different solvent phases and the experimental UV-visible spectral data for I in different solvent environments are presented in Table 8. The combined UV-visible absorption spectrum of the sample of I is shown in Fig. 6. The experimental wavelengths [2] of I in acetonitrile, methanol, and water together with acetone were used for interpretation. The interpretation of the observed spectral features is greatly assisted by molecular orbital calculations, which provide orbital energies and furnish a detailed description of the orbitals, including spatial characteristics, nodal patterns, and the contributions of individual atoms. The atomic orbital components of the frontier molecular orbitals are shown in Fig. 7. The spatial distributions of molecular orbitals, especially those of the highest occupied molecular orbital (HOMO) and the lowest unoccupied molecular orbital (LUMO), are excellent indicators of electron transport in molecular systems. From the computational results for compounds I and II, it is clear that the HOMO is molecular orbital no. 53 with A symmetry, and the LUMO is molecular orbital no. 54 with the same A symmetry. The low value of the HOMO–LUMO gap 253.3 kJ mol^{-1} (Table S3 of the ESM) for I compared to those for II (294.7 kJ mol^{-1}) and III (302.6 kJ mol^{-1}) reflects the chemically reactive [43] nature of I.

The UV-visible spectrum of I was measured in acetone solution, and a very strong absorption band with reduced energy centered on the long wavelength of 309 nm (Table 8) was observed. This band is primarily due to the HOMO→LUMO transition, which corresponds to the characteristic peak of the phenyl ring system due to n–π^* transition. A TD-DFT calculation shows that the corresponding band lies at 292 nm, and has very high values of the oscillator strength (0.461), CI expansion coefficient (0.640), and total free energy −1788678 kJ mol^{-1}. This transition shows a redshift of about 17 nm. From Fig. 7, we can see that the electron density of the HOMO in the heterocyclic ring is larger than that of the LUMO. This suggests that the transition from HOMO to LUMO could lead to intramolecular charge transfer from the heterocyclic ring to the benzene ring. As for the LUMO orbital, the electron density is concentrated on N_{13}–C_{12}–C_1–C_2, so the transition from the HOMO to the LUMO could lead to torsional motion around the C_1–C_{12} bond and lengthening of the C_1–C_{12} bond. Due to the substantial electron transfer from the HOMO to the LUMO, the N_{13}–N_{14} bond shortens. This is due to the effect of torsional vibrations of different bonds as well as electronic charge localization. The calculated absorption band near 282 nm (acetonitrile) in the UV-visible spectrum results from the electron moving from

Table 8 Calculated and experimental electronic absorption spectral data for triazinone derivatives with different solvents

Solvents	Metamitron						Isometamitron							
	Dipole moment	Excitation	CI expansion coefficient	Calculated wavelength (nm)	Oscillator strength[a]	Total free energy (kJ mol^{-1})	Dipole moment	Excitation	CI expansion coefficient	Calculated wavelength (nm)	Oscillator strength[a]	Total free energy	Experimental wavelength (nm) for metamitron	Assignments
Vacuum	3.788	H→L	0.641	293	0.459	−1788662	4.956	H→L	0.640	295	0.314	−1788667	–	n→π*
		H-2→L	0.669	281	0.014			H-1→L	0.573	283	0.076		–	π→π*
		H-3→L	0.612	241	0.011			H-4→L	0.595	249	0.004		–	–
Acetone	3.705	H→L	0.640	292	0.461	−1788678	4.842	H→L	0.640	295	0.326	−1788684	309	n→π*
		H-2→L	0.670	282	0.015			H-1→L	0.637	283	0.073		–	π→π*
		H-3→L	0.654	241	0.013			H-4→L	0.605	250	0.003		218	–
Acetonitrile	3.749	H→L	0.640	293	0.460	−1788656	4.902	H→L	0.640	295	0.320	−1788662	312[f]	n→π*
		H-2→L	0.670	282	0.015			H-2→L	0.541	283	0.074		265[f]	π→π*
		H-3→L	0.642	241	0.012			H-4→L	0.601	250	0.003		–	–
Benzene	3.171	H→L	0.621	297	0.474	−1788646	4.045	H→L	0.619	297	0.371	−1788653	–	n→π*
		H-2→L	0.674	285	0.017			H-2→L	0.607	278	0.068		–	π→π*
		H-3→L	0.639	242	0.020			H-4→L	0.636	253	0.005		–	–
Chloroform	3.450	H→L	0.636	295	0.471	−1788661	4.468	H→L	0.636	296	0.354	−1788667	–	n→π*
		H-2→L	0.672	283	0.016			H-2→L	0.672	281	0.074		–	π→π*
		H-3→L	0.650	242	0.017			H-4→L	0.627	251	0.004		–	–
Dichloromethane	3.592	H→L	0.640	295	0.470	−1788671	4.678	H→L	0.640	296	0.343	−1788677	–	n→π*
		H-2→L	0.671	282	0.016			H-2→L	0.670	282	0.073		–	π→π*
		H-3→L	0.655	242	0.015			H-4→L	0.617	250	0.004		–	–
Ethanol	3.723	H→L	0.640	294	0.462	−1788681	4.863	H→L	0.640	295	0.325	−1788686	–	n→π*
		H-2→L	0.670	282	0.015			H-2→L	0.616	283	0.074		–	π→π*
		H-3→L	0.651	241	0.013			H-4→L	0.604	250	0.004		–	–
Methanol	3.747	H→L	0.640	293	0.457	−1788682	4.895	H→L	0.640	295	0.325	−1788687	312[f]	n→π*
		H-2→L	0.669	282	0.015			H-2→L	0.616	283	0.074		264[f]	π→π*
		H-3→L	0.645	241	0.012			H-4→L	0.604	250	0.004		–	–
Water	3.788	H→L	0.641	293	0.459	−1788662	4.956	H→L	0.640	295	0.314	−1788667	306[f]	n→π*
		H-2→L	0.669	281	0.015			H-1→L	0.573	283	0.076		261[f]	π→π*
		H-3→L	0.612	241	0.012			H-4→L	0.595	249	0.004		–	–

L: no. 54 LUMO orbital, H: no. 53 HOMO orbital

[a] From [2]

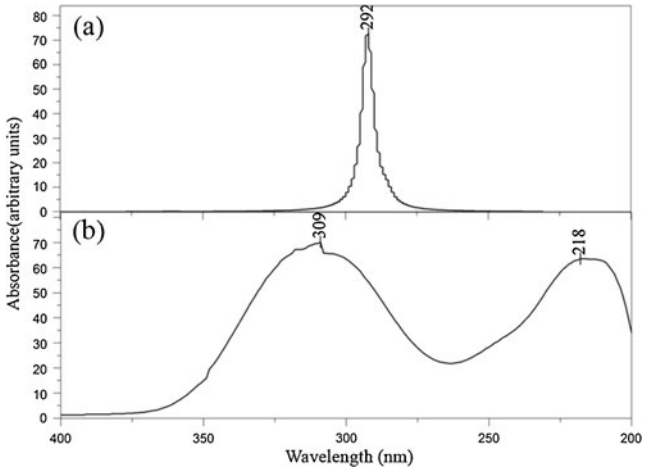

Fig. 6 Combined UV-visible absorption spectrum of metamitron: **a** computed, **b** experimental

the initial state, which is mainly contributed by the HOMO-2, to the final state, which is contributed by the LUMO. The HOMO and LUMO plot shows that both the HOMO and the LUMO orbitals are predominantly localized on the heterocyclic ring, phenyl ring, methyl group, and amino group. Analysis of the electron density of the HOMO and the LUMO can throw some light on the ground and excited state proton transfer process. Both the HOMO and LUMO are π-type orbitals. The HOMO predicts that the intramolecular hydrogen-bonded ring system primarily has bonding character over the N_{19}–H_{25} and C_{17}–N_{16} atoms, whereas it has anti-bonding character over C_{15} (Fig. 7). The oxygen atom (O_{20}) has bonding character, with a large electron density (1.974 e) (Table S2; ESM) present over C_{19}=O_{20}. The electronic charge distribution of the LUMO within the heterocyclic ring shows that the C_{15}–N_{16} position has bonding character, whereas N_{13}–N_{14}, C_{12}–N_{13} and C_{15}–N_{16} have antibonding character. The first dipole-allowed transition was calculated to occur at 293 nm (H→L) (Table 8) in the gas phase, with a strong oscillator strength of 0.459 and a very high CI expansion coefficient (0.641). The next transitions are at 281 nm (H-2→L) and 241 nm (H-3→L) , with much lower oscillator strengths. The redshifts in the solvents acetonitrile, methanol, and water are 19, 19, and 13 nm, respectively. The next transition is at 282 nm (H-2→L) , which has a much lower oscillator strength. The experimental UV-visible spectrum shows a weak π–π* transition at 265 nm in the acetonitrile environment, suggesting a blueshift of 17 nm; it is 18 nm in methanol and 20 nm in water. Because of solvent interference, the experimental π–π* transition is not available in acetone.

In II, the electron density of the HOMO in the heterocyclic ring is also larger than the LUMO; hence the transition is from the heterocyclic ring to the benzene ring. Due to substantial electron transfer from the HOMO to the LUMO, the N_{13}–N_{14} bond shortens. The HOMO diagram shows antibonding character around the benzene ring. It also shows a much higher electron density on the CH_3 group than the HOMO of I. The first intense dipole-allowed transition is calculated to occur at 295 nm (H→L) in vacuum through a number of transitions with high oscillator strength (0.3144), followed by weak transitions at 283 (H-1→L) and 249 nm (H-4→L) with weak oscillator strength. In the case of an acetone environment, a strong transition is observed at 295 nm (H→L) with an oscillator strength of 0.326. This shift in wavelength does not agree with the trend in the polarities of the organic solvents, so it must be the result of a combination of several solvent characteristics, such as polarity, basicity, and hydrogen-bond accepting ability.

Charge distributions

The Mulliken and natural charges of the triazinone derivatives (I, II, and III) computed at the DFT level are collected in Table S1 of the ESM. The charge at the C_{17}/C_{14}/C_6 atom of the carbonyl group is positive due to the negative nature of the O atom, and this influence is related to the aromaticity factor, hydrogen bonding, etc., as discussed earlier. The nitrogen atom is electron-withdrawing in nature, so the charge at the nitrogen site (N_{13}/ N_{17}/ N_3) is negative in I, II, and III. The phenyl ring carbon atoms C_2, C_3, C_4, C_5, and C_6 have negative charges, since each carbon atom is attached to a hydrogen atom. The greatest charge occurs at H_{11} (in I), which is involved in weak C–H…O hydrogen bonding (0.180 e), followed by H_7 (in II), which is also involved in hydrogen bonding. The nitrogen atoms involved in the N–H…O (N_{19}/N_{19}/N_7) hydrogen bonding have the highest negative Mulliken charges (−0.555, −0.567, and −0.540 e) in the triazinone derivatives. The charge analysis shows that the presence of the electronegative nitrogen atom (N_{19}/N_{19}/N_7) imposes highly positive charges on the hydrogen atoms of the amino group. The largest positive charges occur at H_{24} and H_{25}, which are involved in strong N–H…O hydrogen bonding, with Mulliken charges of 0.390 and 0.411 e in I, 0.392 and 0.417 e in II, and 0.402 e in III, respectively. The quantitative relation is that the increase in charge at the hydrogen atoms, especially those taking part in hydrogen bonding (as supported by NBO analysis), is a clear manifestation of the strength of hydrogen bonding.

Electrostatic potential

It is well established that the electrostatic potential created by the nuclei and electrons of a molecule in the surrounding space provides a useful tool for interpreting

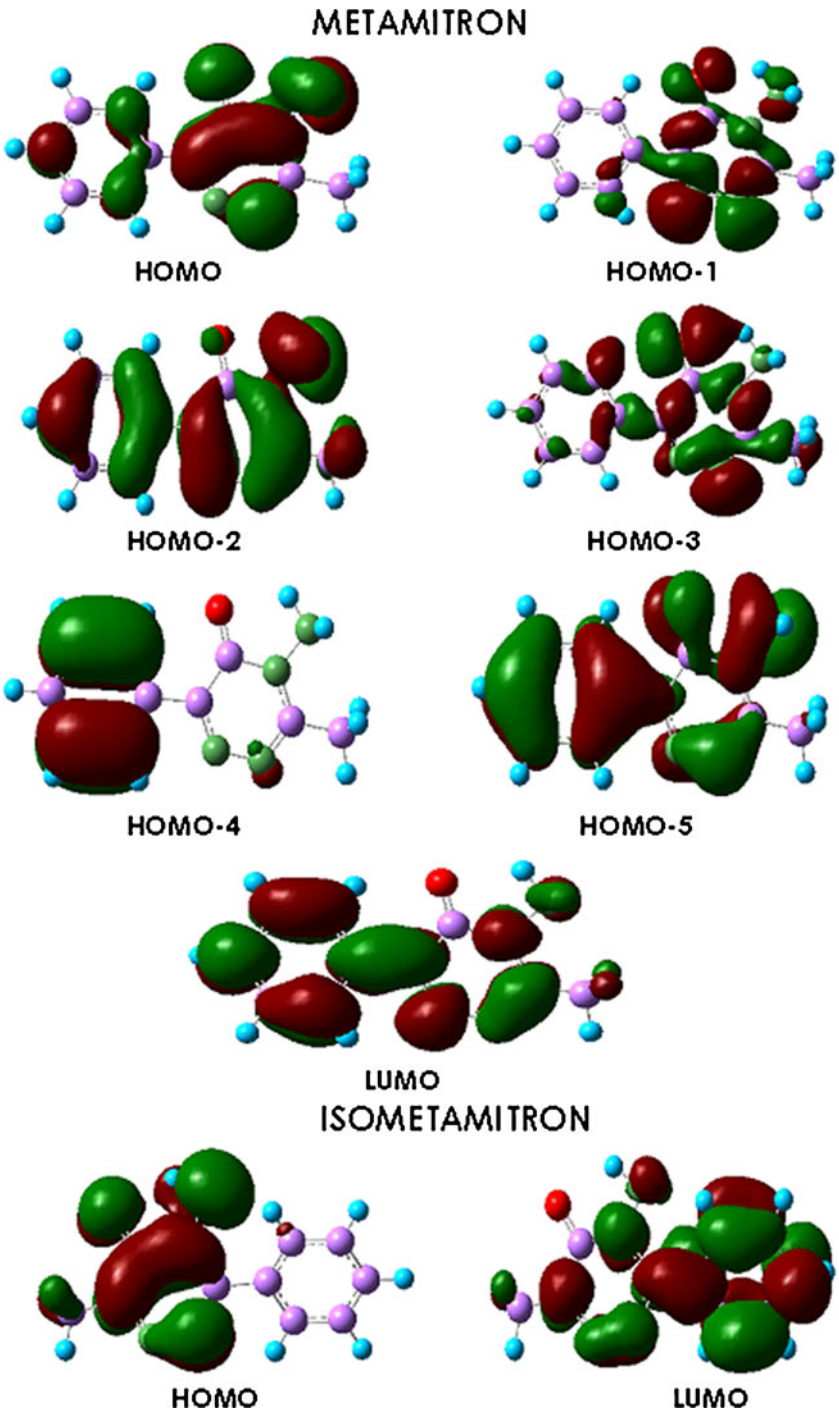

Fig. 7 HOMO and LUMO plots for triazinone derivatives

and predicting molecular behavior. Indeed, it has been shown to be most helpful when studying both electrophilic and nucleophilic processes, and is particularly well suited to studies that involve the identification of key features necessary for the "recognition" of one molecule by another. The molecular surface electrostatic potential (MSEP) is rigorously defined as the first-order interaction between a positive unit charge at any point in the vicinity of a molecule and the charge distribution contributed by both electrons and nuclei. The potential $V(r)$ can be calculated through Eq. 3 [44]:

$$V(\mathrm{r}) = \sum_{A} \frac{Z_A}{|R_A - \mathrm{r}|} - \int \frac{\rho(\mathrm{r}')\mathrm{d}\mathrm{r}'}{|\mathrm{r}' - \mathrm{r}|}, \tag{3}$$

where Z_A is the charge on nucleus A at a distance R_A, and $\rho(r)$ is the electronic density function defined by the 0.001 a.u. contour.

The MSEP has been employed as an informative tool in chemistry to describe different physical and chemical features, including noncovalent interactions in complex biological systems. The molecular electrostatic potential (MEP) is the most useful electrostatic property for studying the relation between structure and activity. The three-dimensional MEP energy surfaces, when superimposed over the total electronic density in the triazinone derivatives studied (Fig. 8), show that compounds I, II, and III have almost identical isodensity surfaces, with the potential isocontour surface in and around heterocyclic ring exhibiting two negative energy regions (red color) with charges of between −0.0409 and −0.0500 e. One is located over the oxygen of the carbonyl group and the other is centered on the N=N of the heterocyclic ring. The positive-energy area (white color) with charges of between 0.0500 and 0.0409 e occurs over the hydrogen atoms of both the methyl group and the benzene ring. The red regions indicate areas that would favor interactions with approaching electrophiles. The potential [$V(r)$] minima are in the region of a lone pair in a plane bisecting the HNH angle, thus predicting a hydrogen-bonding acceptor site. The white regions interact extensively with incoming nucleophiles, and are thus the sites of hydrogen-bond donor groups.

Bioactivity

Theoretical investigations of Dornow et al. [45] supplied the background for the discovery of the group of herbicides with an asymmetric triazine skeleton. Owing to their similarity to nucleic acids, a series of 1,2,4-triazinone compounds were synthesized and tested for biological activity [46]. The most active member of the group is 4-amino-3-methyl-6-phenyl-1,2,4-triazin-5-one, introduced under the common name metamitron (I), which is a selective pre- and post-emergence herbicide and is suitable for selective weed control in sugar beet and red beet. Metribuzin is crystalline in nature and very slightly soluble in water, but it is relatively soluble in organic solvents like methanol. It is effective towards many broad-leaved weeds, including hard-to-control weeds.

Stephan Wilski et al. [47] studied herbicide binding in various mutants of the D1 protein of photosystem II of *Chlamydomonas reinhardtii*. For 1,2,4-triazin-5-ones, Ser264Lys and Ser264Ile mutants were selected after a series of mutant studies. Through molecular modeling studies of metribuzin-type compounds, it was shown that replacing the thiomethyl group with a thiol group leads to tighter binding and increases the binding affinity of the compound. For metamitron-type compounds, the presence of NH_2 was found to be necessary for higher activity, even though the benzene ring is most favorable. Other alicyclic groups also show good activities, but replacement with an electron-donating methyl group reduces the activity.

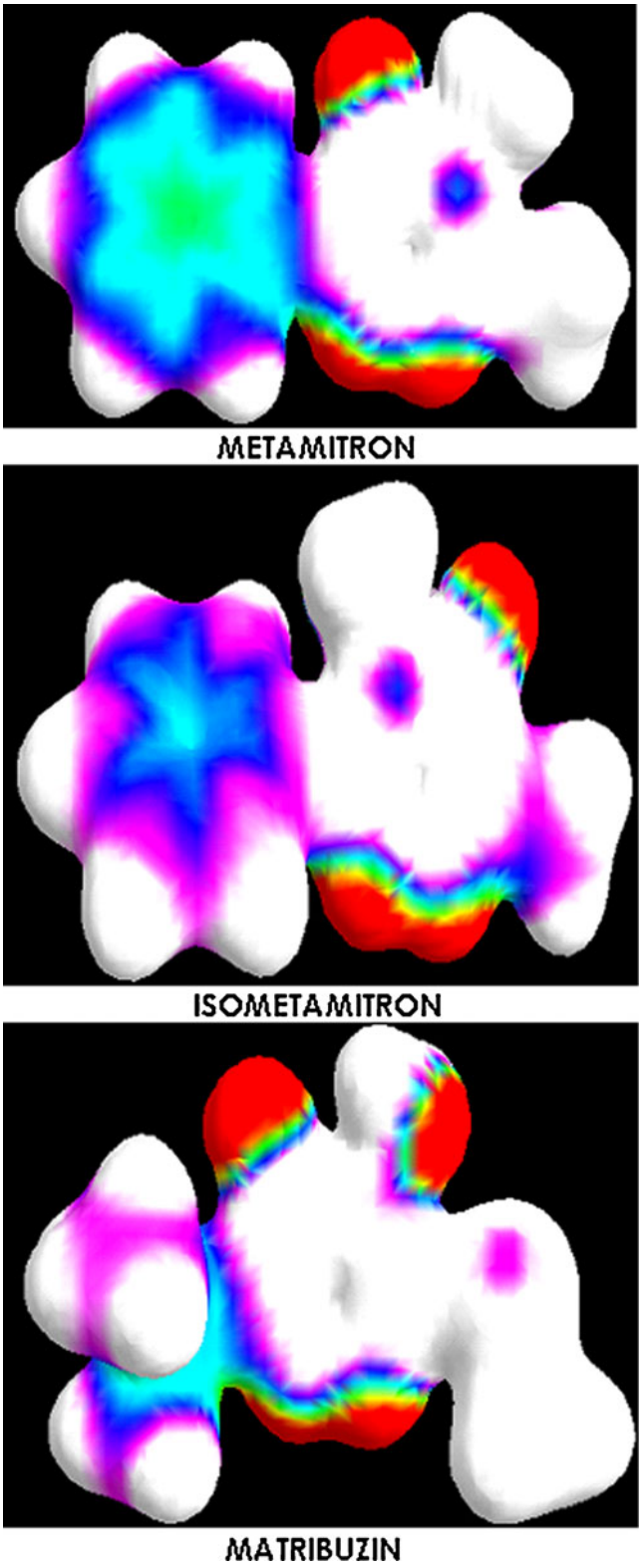

Fig. 8 Electrostatic potential plots for the triazinone derivatives

The present study demonstrates the importance of the N–C=O group to the bioactivity, since it is the place where strong intramolecular (monomer) and intermolecular hydrogen

bonds (dimer) are observed. Hydrogen-bond interactions decide the nature and properties of biomolecules and proteins. Thus, any factor that favors strong intermolecular hydrogen bonding with the amino acid residues of the D1 protein [47] enhances binding, which results in the inhibition of photosynthesis. Since interactions with proteins are "lock and key" in nature, other structural features that aid proper docking at the interaction site are crucially important. Even the improper-type hydrogen bond C–O…H has a comparatively small strength, and its presence causes multiple hydrogen bond formation with varying acceptor and donor groups of proteins. The strong binding of herbicides to the Qb site [47] is an essential condition for herbicidal activity, but it reduces photosynthesis in all kinds of plants.

Conclusions

The aromaticities and equilibrium geometries of the monomeric and dimeric structures of triazinone derivatives were determined and analyzed at the DFT level. Vibrational wavenumbers and infrared and Raman intensities calculated at the BLYP/6-311 G (df, p) level agreed well with the corresponding experimental data. The optimized geometry shows that both of the H atoms of the amino group are pushed aside (out of plane) with respect to the plane of the heterocyclic ring. The planarity of the triazinone molecule is distorted due to the interactions of the nitrogen, oxygen, and methyl groups in the ring, including hydrogen-bond formation. The potential C=O…H–C bond, the loss of planarity, and the development of asymmetry in the benzene ring limit the delocalization in the heterocycles of the triazinone derivatives with a phenyl ring.

NBO analysis reveals that the redshifting of the N–H stretching wavenumber exaggerates the decrease in N–H bond order values that occurs due to donor–acceptor interactions. This leads to the stability and in turn to the bioactive nature of the triazinone herbicides. Due to intra- and intermolecular N–H…O and C–H…O hydrogen bonding, there is an increase in the charge density of the antibonding orbital of the N–H bond, electron density delocalization, an increase in the N–H bond distance, and a concomitant decrease in the vibrational stretching wavenumber. There is also a decrease in the electron density, in the stabilization energy, in the C–H bond length, and an increase in the stretching wavenumber. H-bonding leads to a decrease in the NH_2 stretching wavenumber, an increase in the NH_2 bending wavenumber, and an increase in IR intensity. Due to strong intermolecular hydrogen bonding, these molecules show enhanced herbicidal activity. The potential [$V(r)$] minima occur in the region of a lone pair in a plane bisecting the HNH angle, thus predicting a site of hydrogen-bonding acceptors. The predicted electronic absorption spectra from TD-DFT calculations have been analyzed in combination with the PCM models for various solvents and compared with the experimental UV-visible spectrum, and they were found to mainly derive from the contributions of the n–π* and π–π* bands. The decrease in the HOMO–LUMO energy gap clearly explains the charge-transfer interactions that take place within these molecules and lead to their enhanced herbicidal activity.

Acknowledgments The author D. Arul Dhas thanks the University Grants Commission (UGC), India, for the award of a Teacher Fellowship under Faculty Improvement Program (FIP) scheme leading to the Ph.D. degree.

References

1. Macounova K, Urban J, Krysova H, Krysa J, Jirkovsky J, Ludvik J (2001) Photodegradation of metamitron (4-amino-6-phenyl-3-methyl-1,2,4-triazin-5(4H)-one) on TiO_2. J Photochem Photobio A Chem 140:93–98
2. Palm WU, Millet M, Zetzsch C (1997) Photochemical reactions of metamitron. Chemo 35:1117–1130
3. Farzinnejad N, Miran Beig AA, Fotouhi L, Torkestan K, Ghadirian HA (2005) Electrochemical behavior of some triazine derivatives at glassy carbon electrode in non-aqueous media. J Electroan Chem 580:245–254
4. Muszkat L (1998) Pesticide remediation in soils and water. In: Kearney P, Roberts T (eds) Photochemical processes. Wiley, Chichester, pp 307–337
5. Sancho D, Vega M, Deban L, Pardo L, Barrado E (1999) Electrochemical determination of the effect of lead(II) on the photochemical degradation of the pesticide metamitron. Toxicol Environ Chem 68:259–266
6. Parlar H, Pletsch B (1988) Mechanism of the photoinduced deamination reaction of aminotriazinon herbicides. Chemo 17:2043–2048
7. Moros J, Armenta S, Garrigues S, de la Guardia M (2006) Quality control of Metamitron in agrochemicals using Fourier transform infrared spectroscopy in the middle and near range. Anal Chim Acta 565:255–260
8. Takhashi O, Kohno Y, Saito K (2003) Molecular orbital calculations of the substituent effect on intermolecular CH/π interaction in C_2H_3X–C_6H_6 complexes (X = H, F, Cl, Br, and OH). Chem Phys Lett 378:509–515
9. Stevens MF, Schwalbe CH, Patel N, Gate EN, Bryant PK (1995) Structural studies on bioactive compounds. Part 26. Hydrogen bonding in the crystal structure of the N-methylformamide solvate of the immunomodulatory agent 2-amino-5-bromo-6-phenylpyrimidin-4-one (bropirimine): implications for the design of novel anti-tumour strategies. Anticancer Drug Des 10:203–213
10. Altomare C, Tasi RS, El Tayari N, Testa B, Carotti A, Cellamare S, De Benedetti PG (1991) Determination of lipophilicity and hydrogen-bond donor acidity of bioactive sulfonyl-containing compounds by reversed-phase HPLC and centrifugal partition chromatography and their application to structure–activity relations. J Pharm Pharmacol 43:191–197
11. Creighton TE (1984) Proteins, structure and molecular principles. Freeman & Co, New York
12. Arul Dhas D, Hubert Joe I, Roy SDD, Freeda TH (2010) DFT computations and spectroscopic analysis of a pesticide: chlorothalonil. Spectrochim Acta A 77:36–44

13. Ludvik J, Urban J, Fabry J, Cisarova I (2007) 4-Amino-3-methyl-6-phenyl-1,2,4-triazin-5(4H)-one (metamitron) and 4-amino-6-methyl-3-phenyl-1,2,4-triazin-5(4H)-one (isometamitron). Acta Cryst C 63:259–262. doi:10.1107/S0108270107009596/gg3068Isup2.hkl
14. Frisch MJ et al (2004) Gaussian 03, revision C.02. Gaussian, Inc., Wallingford
15. Alecu IM, Zheng J, Zhao Y, Truhlar DG (2010) Computational thermochemistry: scale factor databases and scale factors for vibrational frequencies obtained from electronic model chemistries. J Chem Theor Comput 6:2872–2887
16. Jamroz MH (2004) Vibrational energy distribution analysis: VEDA 4.0 program. Drug Institute, Warsaw
17. Keresztury G (2002) Raman spectroscopy theory. In: Chalmers JM, Griffith PR (eds) Handbook of vibrational spectroscopy, vol 1. Wiley, New York, pp 71–87
18. Glendening ED, Reed AE, Carpenter JE, Weinhold F (1998) NBO, version 3.1 TCI. University of Wisconsin, Madison
19. Reed AE, Curtiss LA, Weinhold F (1988) Intermolecular interactions from a natural bond orbital, donor–acceptor viewpoint. Chem Rev 88:899–926
20. Cossi M, Barone V, Cammi R, Tomasi J (1996) Ab initio study of solvated molecules: a new implementation of the polarizable continuum model. Chem Phys Lett 255:327–335
21. Chopra D, Mohan TP, Rao KS, Guru Row TN (2005) 6-*Tert*-butyl-4-isopropylideneamino-3-methylsulfanyl-1,2,4-triazin-5(4H)-one. Acta Cryst E61:1112–1114
22. Miranda MS, Matos MAR, Morais VMF, Liebman JF (2011) Study of energetics and structure of 1,2,3-benzotriazin-4(3H)-one and its 1H and enol tautomers. J Phys Chem B 115:6616–6622
23. Jeffrey GA (1997) Introduction to hydrogen bonding. Oxford University Press, New York
24. Colthup NB, Daly LH, Wiberley SE (1990) Introduction to infrared and Raman spectroscopy. Academic, New York
25. Smith B (1999) Infrared spectral interpretation: a systematic approach. CRC, Washington, DC
26. Del Zoppo M, Castiglioni C, Zuhani P, Zerbi G (1997) The vibrational approach to determine molecular nonlinearities: what do we learn from the method and the data? Synth Met 85:1043–1046
27. Ruiz Delgado MC, Hernandez V, Casado J, Lopez Navarrete JT, Raimundo JM, Blanohard P, Roncali J (2003) Vibrational and quantum-chemical study of push–pull chromophores for second-order nonlinear optics from rigidified thiophene-based π-conjugating spacers. Chemistry 9:3670–3682
28. Maroulis G (2003) Electric multipole moment, dipole and quadrupole (hyper)polarizability derivatives for HF ($X^1\Sigma^+$). J Mol Struct Theochem 633:177–197
29. Bellamy LJ (1975) The infrared spectra of complex molecules, vols. 1 and 2. Chapman and Hall, London
30. Marques MPM, Amorim-da-Costa AM, Ribeiro-Claro PJA (2001) Evidence of C–H…O hydrogen bonds in liquid 4-ethoxybenzaldehyde by NMR and vibrational spectroscopies. J Phys Chem A 05:5292–5297
31. Ribeiro-Claro MMPM, Amorimda Costa AM (2002) Experimental and theoretical evidence of C–H…O hydrogen bonding in liquid 4-fluorobenzaldehyde. Chem Phys Chem 3:599–606
32. Varsanyi G (1969) Vibrational spectra of benzene derivatives. Academic, New York
33. Hernandz V, Castiglioni C, Zerbi G (1994) Hyperconjugation from infrared intensities: the case of methyl acetate and of its selectively deuterated derivatives. J Mol Struct 324:189–198
34. Lin-Vien D, Colthup NB, Fatelel WG, Grasselli GJ (1991) The handbook of infrared and Raman characteristic frequencies of organic molecules. Academic, New York
35. Chohan ZH, Sumrra SH, Youssoufib MH, Hadda TB (2010) Metal based biologically active compounds: design, synthesis, and antibacterial/antifungal/cytotoxic properties of triazole-derived Schiff bases and their oxovanadium(IV) complexes. Eur J Med Chem 45:2739–2747
36. Liu JN, Chen ZR, Yuan SF, Zhejiang J (2005) Study on the prediction of visible absorption maxima of azobenzene compounds. Univ Sci B 6:584–589
37. Yang Y, Zhang W, Gao X (2006) Blue-shifted and red-shifted hydrogen bonds: theoretical study of the CH_3CHO…HNO complexes. Int J Quantum Chem 106:1199–1207
38. Herrebout WA, Melikova SM, Delanoye SN, Rutkowski KS, Shchepkin DN, van der Veken BJ (2005) A cryosolution infrared study of the complexes of fluoroform with ammonia and pyridine: evidence for a C−H…N pseudo blue-shifting hydrogen bond. J Phys Chem A 109:3038–3044
39. Janiak C, Scharmann TG (2003) Supramolecular C-H…O, C–H…N and C–H…Cl interactions in metal compounds with multi-topic poly (pyrazolyl) borate ligands. Polyhedron 22:1123–1133
40. Matsuura H, Yoshida H, Hieda M, Yamanaka SY, Harada T, Kei SY, Ohno K (2003) Experimental evidence for intramolecular blue-shifting C−H…O hydrogen bonding by matrix-isolation infrared spectroscopy. J Am Chem Soc 125:13910–13911
41. Harada T, Yoshida H, Ohno K, Matsuura H (2002) Conformational stabilities of 1-methoxy-2-(methylthio)ethane and relevant intramolecular CH...O interaction studied by matrix-isolation infrared spectroscopy and density functional calculations. Chem Phys Lett 362:453–460
42. Alabugin IV, Manoharan M, Peabody S, Weinhold F (2003) The electronic basis of improper hydrogen bonding: a subtle balance of hyperconjugation and rehybridization. J Am Chem Soc 125:5973–5987
43. Mills NS, Levy A, Plummer BF (2004) Antiaromaticity in fluorenylidene dications. Experimental and theoretical evidence for the relationship between the HOMO/LUMO gap and anti-aromaticity. J Org Chem 69:6623–6633
44. Mishra S, Chaturvedi D, Kumar N, Tandon P, Siesler HW (2010) An ab initio and DFT study of structure and vibrational spectra of γ form of oleic acid: comparison to experimental data. Chem Phys Lip 163:207–217
45. Dornow A, Menzel H, Marx M (1964) Synthesen stickstoffhaltiger Heterocyclen, XXVII. Uber 1.2.4-Triazine, I Darstellung einiger neuer s-Triazolo[3.2-c]-as-triazine. Chem Ber 97:2173–2178
46. Schmidt RR, Draber W, Eue L, Timmler H (1975) Herbicidal activity and selectivity of new 3-alkyl-4-amino-6-aryl-1,2,4-triazin-5-ones. Pestic Sci 6:239–244
47. Wilski S, Johanningmeier U, Hertel S, Oettmeier W (2006) Herbicide binding in various mutants of the photosystem II D1 protein of *Chlamydomonas reinhardtii*. Pest Biochem Physiol 84:157–164